Kilauea slow slip events: Identification, source inversions, and relation to seismicity

E. K. Montgomery-Brown,[1,2] P. Segall,[1] and A. Miklius[3]

[1] Several slow slip events beneath the south flank of Kilauea Volcano, Hawaii, have been inferred from transient displacements in daily GPS positions. To search for smaller events that may be close to the noise level in the GPS time series, we compare displacement fields on Kilauea's south flank with displacement patterns in previously identified slow slip events. Matching displacement patterns are found for several new candidate events, although displacements are much smaller than previously identified events. One of the candidates, 29 May 2000, is coincident with a microearthquake swarm, as are all of the previously identified slow slip events. The microearthquakes follow the onset of slow slip, implying that they are triggered by stress changes during slip. The new slow slip event brings the total number of events on Kilauea, between 1997 and 2007, to eight, the smallest having $M_W = 5.3$, and the largest having $M_W = 6.0$. While the recurrence time between the four largest events is 2.11 ± 0.01 years, the repeat time for all eight events is 0.9 ± 0.6 years. We invert for the fault geometry and distribution of slip during the slow slip events. The optimal source depths of 5 km, assuming uniform slip dislocations in an elastic half-space, are considerably shallower than the accompanying swarm earthquakes (6.5–8.5 km), which would place the earthquakes in a zone of decreased Coulomb stress. Inversions including the effects of topography and layered elastic structure in the forward models favor depths comparable to microearthquake depths, such that the earthquakes are located in a region of increased Coulomb stress. We also invert for time-dependent fault slip directly from the 30 s GPS phase observations, constraining the source to the optimal uniform slip geometry. On the basis of these inversions, the larger events last between 1.5–2.2 days. The data are unable to resolve migration of slip along the fault. The temporal pattern of accompanying microearthquakes is consistent with the fault slip history assuming a seismicity rate theory based on rate and state-friction, making the swarm earthquakes coshocks and aftershocks of the slow slip events.

1. Introduction

[2] Several slow slip events on Kilauea Volcano's southern flank were recently discovered using Global Positioning System (GPS) data [*Cervelli et al.*, 2002; *Segall et al.*, 2006; *Brooks et al.*, 2006]. Slow slip events have also been observed by GPS networks worldwide in a variety of plate boundary environments including the Bungo Channel in southwestern Japan [*Hirose et al.*, 1999; *Ozawa et al.*, 2004; *Miyazaki et al.*, 2003; *Ozawa et al.*, 2001], the Tokai region of Japan [*Heki and Miyazaki*, 2001; *Miyazaki et al.*, 2006], Cascadia on the western coast of the USA and Canada [*Dragert et al.*, 2004; *Rogers and Dragert*, 2003], and

Guerrero in southern Mexico [*Yoshioka et al.*, 2004; *Larson et al.*, 2004; *Lowry et al.*, 2001; *Kostoglodov et al.*, 2003]. Slow slip events have durations of days to years, are observed at the Earth's surface by geodetic instruments, and are sometimes correlated with small bursts of coherent seismic energy in the 1–10 Hz band termed nonvolcanic tremor. Periodic recurrence has been observed for some slow slip events with the most striking example being the 14-month repeat period for the slow slip events beneath Vancouver Island [*Miller et al.*, 2002]. *Szeliga et al.* [2004] and *Brudzinski and Allen* [2007] additionally note three different periodicities of slow slip events along the Cascadia subduction zone: the previously mentioned 14-month period in the North, a 19-month period through Oregon, and 10 months in southern Oregon and northern California. *Schwartz and Rokosky* [2007] summarized circum-Pacific observations of slow slip events and their associated seismic signals.

[3] On Kilauea Volcano, a sequence of slow slip events large enough to be detected visually from the GPS time series have been identified [*Cervelli et al.*, 2002; *Segall et al.*, 2006;

---

[1]Department of Geophysics, Stanford University, Stanford, California, USA.

[2]Formerly E.K. Desmarais.

[3]U.S. Geological Survey, Hawaii National Park, Hawaii, USA.

Table 1. Catalog of Previously Identified and Possible Slow Slip Events[a]

Event Date	Year	Month	Day	$2005 - \theta$ (rad)	$2003 - \theta$ (rad)	Probability[b]	EQ Ratio	Reference
1998.7164	1998	9	19	0.56	1.03	>0.999	3.1	1,2
1999.0260	1999	1	10	1.00	-	0.55	0.71	
2000.4084	2000	5	29	0.79	0.99	0.75	7.15	New
2000.8566	2000	11	9	0.52	0.87	>0.999	1.8	1,2,3
2001.7164	2001	9	19	0.99	1.07	0.55	1.36	
2002.9603	2002	12	17	0.67	-	0.96	1.1	2
2005.0699	2005	1	26	0.54	0.84	>0.999	10.5	1,2
2005.4863	2005	6	27	0.98	1.07	0.56	1.06	
2007.2890	2007	4	16	0.99	1.01	0.55	0.83	
2007.4617	2007	6	18	0.89	0.93	0.68	N/A	4[c]
1998.1384	1998	2	20	0.89	0.79	0.85	2.75	2
1999.3191	1999	4	27	-	1.06	0.7	0.37	
1999.8890	1999	11	21	0.87	0.78	0.85	4	2
2003.4945	2003	7	3	-	0.55	0.99	2.75	1,2
2004.3456	2004	5	6	-	1.06	0.7	1.7	
Average Velocity	-	-	-	0.91	2.0	0.65	-	-

[a]Citations for previously identified slow slip events: 1, *Segall et al.* [2006]; 2, *Brooks et al.* [2006]; 3, *Cervelli et al.* [2002]; 4, *Montgomery-Brown et al.* [2007]; and 5, *Brooks et al.* [2007]. Angles (θ) are reported for the candidate events that exceed the threshold to be considered a possible slow slip event similar to either the 2005 and 2003 reference events. Both angles are reported if the candidate event's angle exceeds both thresholds, and the events are grouped by which event was most similar. Probabilities presented indicate the likelihood that the candidate event is a slow slip event.

[b]Probabilities based on correlation with the most similar slow slip event reference.

[c]The event in 2007 is not studied here because of its close association with a large dike intrusion.

Brooks et al., 2006]. Times of the seven previously identified slow slip events are listed in Table 1 denoted with citations. A subset of four of the slow slip events were noted to exhibit a 774 ± 7 days (2.11 ± 0.01 years) recurrence time by *Brooks et al.* [2006].

[4] Strong temporal correlations have been observed between slow slip events and nonvolcanic tremor in various subduction zones suggesting that the signals are related [*Rogers and Dragert*, 2003; *Obara et al.*, 2004; *Ozawa et al.*, 2004; *Payero et al.*, 2008]. While some researchers have proposed that tremor results from fluid flow [*Kao et al.*, 2005; *Rogers and Dragert*, 2003], *Shelly et al.* [2006] showed that 80% of the tremor was composed of waveforms from known low-frequency earthquakes. These low-frequency earthquakes were shown to have shear faulting mechanisms with the same orientation as large subduction events in the area [*Ide et al.*, 2007]. However, nonvolcanic tremor on Kilauea has not been observed to date.

[5] Slow slip events can release strain without radiating significant seismic energy, but these events can be observed with continuously recording geodetic networks. Regardless of duration, any slip causes stress redistribution, which impacts the state of stress on a fault. *Thatcher* [2001] suggested that the stress perturbation from each slow slip event in Cascadia may bring the fault closer to failure. If the fault is near enough to failure, an individual slow slip event may trigger a megathrust, or in the case of Kilauea, a catastrophic landslide [*Moore et al.*, 1994].

[6] *Segall et al.* [2006] and *Brooks et al.* [2006] also noted that each of the Kilauea slow slip events was accompanied by increases in south flank microseismicity, although the cumulative magnitude of these events are far too small to account for the displacements observed at GPS sites. *Segall et al.* [2006] showed that the 2005 slow slip event began before the associated seismic swarm. In addition, they used the seismicity rate theory of *Dieterich* [1994] to show that the temporal evolution of the 2005 swarm was consistent with stress changes due to the 2005 slow slip event, making the swarm events "coshocks" and aftershocks of the slow slip

event. The seismicity rate increased while the slow slip event was in progress and decayed to background levels after the slow slip event finished.

[7] Here we investigate the sequence of slow slip events that occurred on Kilauea since mid-1997. In our investigation we (1) produce a catalog of slow slip event times and displacement patterns of previously identified and newly discovered slow slip events, (2) invert the GPS displacements to determine the depth and spatial distribution of slip, and (3) correlate geodetic observations of these slow slip events with seismicity patterns.

2. Geologic Setting

[8] Kilauea is a shield volcano on the Big Island of Hawaii, and is one of the most active volcanoes on Earth. Kilauea's major volcanic and tectonic features include a summit caldera, rift zones in the East and Southwest, and east-west trending cliffs ("Palis" in Hawaiian) marking the head scarps of the large-offset Hilina normal fault system (Figure 1). Eruptions have been nearly continuous for over 25 years in the East Rift Zone (ERZ), but both the summit and the Southwest Rift Zone continue to deform [*Miklius et al.*, 2005].

[9] Kilauea is a very asymmetric volcano perhaps resulting from volcanic spreading [*Borgia*, 1994] and the concurrent growth of nearby Mauna Loa [*Lipman et al.*, 2006]. Instability due to volcanic spreading has also been suggested as the cause of the many large submarine landslides observed offshore of the Hawaiian Islands [*Moore et al.*, 1994].

[10] Earthquakes clustered on a planar structure at depths between $8-10$ km define a boundary beneath Kilauea's south flank, south of the two rift zones [*Got and Okubo*, 2003]. A planar structure at the same depth was imaged by a shipboard seismic reflection survey spanning several tens of kilometers offshore; the reflections also illuminated what appears to be the toe of a landslide at its southern extent [*Morgan et al.*, 2000]. It has been postulated that this subhorizontal feature is a detachment fault at the contact between the base of the
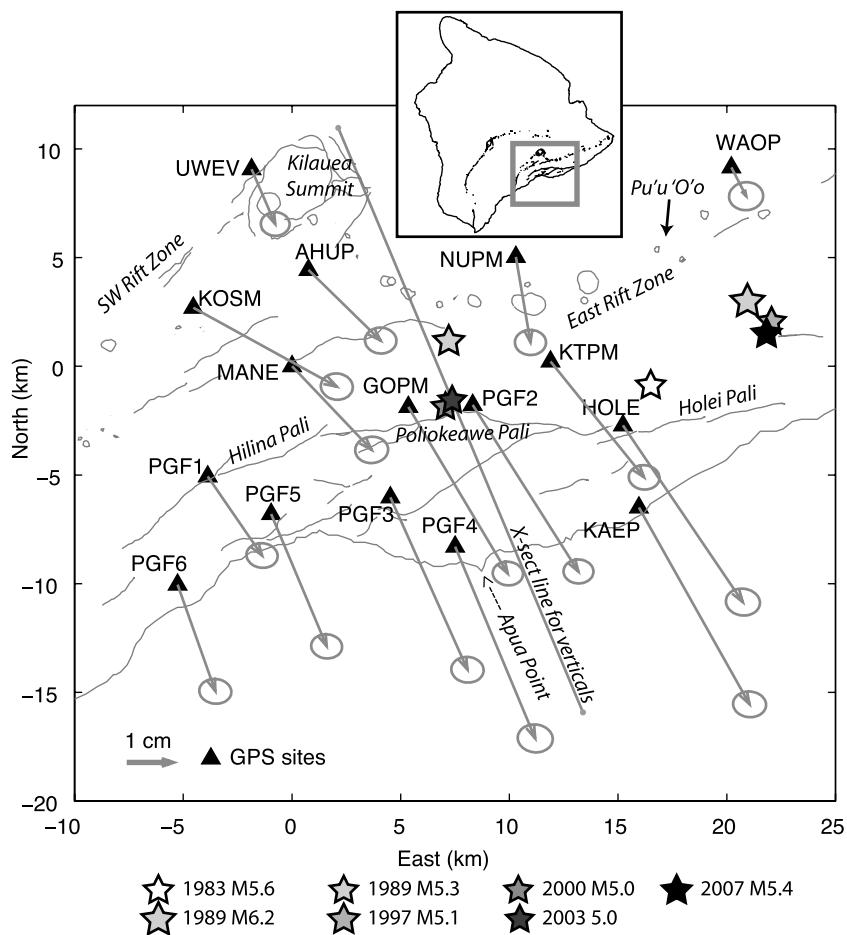
Figure 1. Reference map of Kilauea Volcano showing major tectonic and volcanic features. Average velocities are shown for the continuous GPS sites (black triangles) computed from GPS positions for the year 2001. Stars show locations of M > 5 earthquakes on Kilauea in the last 25 years.

volcanic pile and the much older Cretaceous sea floor sediments [*Hill*, 1969]. It is believed that this detachment is the fault that ruptured during Kilauea's two historic tsunamigenic *M* > 7 earthquakes in 1868 and 1975 [*Ando*, 1979; *Furumoto and Kovach*, 1979; *Lipman et al.*, 1985], although it has been suggested that the 1868 event rupture must have extended beneath Mauna Loa as well [*Wyss*, 1988].

[11] Quasi-steady deformation on the south flank between 1990 and 1996 is well modeled by 21 cm a^{-1} of seaward slip on a nearly horizontal detachment fault extending offshore at 10 km depth and a similar amount of opening in the deep ERZ [*Owen et al.*, 2000b]. Vertical sea floor deformation measurements from 2000 to 2005 show that deformation of the flank continues offshore [*Phillips and Chadwell*, 2004] and the vertical displacements are well-fit by *Owen et al.*'s [2000b] decollement model. Earthquake locations for nearly all midcrustal earthquakes (5–10 km deep) recorded between 1998 and 2004, however, have epicenters between the rift zones and the Palis perhaps implying some variation in physical properties south of the Hilina Pali faults [*Got and Okubo*, 2003]. The larger Hilina fault structures are mainly interpreted to be either (1) deep-rooted faults related to the basal detachment, on the basis of deformation measurements [*Lipman et al.*, 1985] and seismic tomography [*Okubo et al.*, 1997] or (2) shallow listric normal faults, on the basis of fault offsets

and rotated lava flows south of the Palis [*Cannon et al.*, 2001], or slump structures in seismic reflection data [*Morgan et al.*, 2000].

[12] Slow slip events on Kilauea's southern flank have been identified as accelerated southward displacements lasting 2 days, with maximum displacements of up to 2 cm at the coast, localized in the area south of the Hilina Pali faults [*Cervelli et al.*, 2002; *Brooks et al.*, 2006; *Segall et al.*, 2006]. One example time series is shown in Figure 2, while displacement fields due to several slow slip events are shown in Figure 4. Note that stations north of the East Rift Zone (e.g., NUPM and WAOP) displace southward during slow slip events. The displacements at these sites are critical for differentiating slow slip events from rift zone intrusions, which produce displacements away from the rift (i.e., northward at sites north of the rift) [e.g., *Owen et al.* 2000b]. Although coastal sites experience steady-state uplift [*Miklius et al.*, 2005], many of these sites subside during slow slip events (Figure 3).

3. GPS Data Processing

[13] The continuous GPS data analyzed in this paper are from the Kilauea Volcano GPS network, which is collaboratively operated by the Hawaiian Volcano Observatory
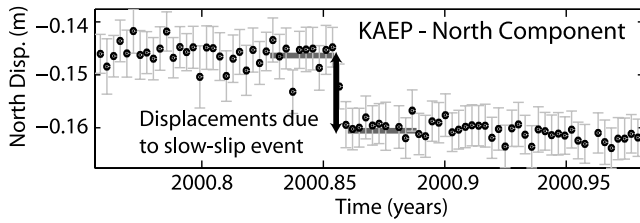
Figure 2. North component of daily GPS position time series at the coastal site KAEP for the November 2000 slow slip event. Mean positions 10 days on either side of a 3-day window, shown by the gray lines, centered on each candidate day to determine offset (black arrow) are used to compute displacements for each slow slip event. Error bars are the scaled formal GIPSY errors.

(HVO), Stanford University, and the University of Hawaii. Daily solutions are computed at HVO using the GIPSY/OASIS II software developed at JPL in precise point positioning mode with nonfiducial orbits [*Zumberge et al.*, 1997; T. Gregorius, GIPSY-OASIS II: How it Works (self-published), 1996, University of Newcastle upon Tyne, New Castle, United Kingdom, available at http://www.ceg.ncl.ac.uk/research/geomatics/geodesy/assets/gipsy-oasisIIHowItWorks.pdf]. After processing, the daily nonfiducial solutions are transformed into a global ITRF2005 reference frame [*Altamimi et al.*, 2007] with a 7 parameter Helmert transformation provided by JPL.

[14] The first post processing step is to remove outliers, defined as any day for which a station's position is more than 2 cm higher or lower than the mean of that station's position for a 5-day window. Typically, this amounts to only a few days of data for each site over the 10-year time span of available data. Intrusions or earthquakes (e.g., intrusions in January 1997 and June 2007) can result in larger mean displacements within a 5-day window. However, no geologic event in this data set, spanning January 1998 to April 2007, produced mean displacements exceeding 2 cm in any 5-day window.

[15] A Kalman filter is used to estimate average station velocities and errors in the daily realization of the GPS reference frame. We estimate and remove an average velocity to highlight deviations from this quasi-steady state. On Kilauea's south flank, some sites display quasi-steady motions of up to 7 cm a^{-1} (Figure 1). To help constrain the reference frame, we include one station each on Mauna Loa, Mauna Kea, Hilo, and Maui, and two sites Oahu; these stations are not included in the following analysis of the slow slip events. Some sites, such as those near Kilauea's summit, have highly variable displacements over time and because of that variability, their average velocity is not meaningful. To estimate the velocity and reference frame corrections, we use the observation equation, modified from *Miyazaki et al.* [2003]:

$$\mathbf{X}(t) = \mathbf{X_o} + L(\mathbf{x}, t - t_o) + \mathbf{v}(t - t_o) + F\mathbf{f}(t) + \epsilon, \quad (1)$$

where $\mathbf{X}$ are the daily positions of each station, $\mathbf{X_o}$ are initial station positions at $t = t_o$, L are random benchmark motions, $\mathbf{v}$ are the average velocities of each station, F is a linearized Helmert transformation, $\mathbf{f}$ is a vector of frame translations and

rotations which are modeled as a white noise process, and ε are the remaining errors and nonlinear motions. At several points in the time series, steps occur because of geologic events, or equipment changes. At these times, we increase the variance of L to a large value, thereby allowing for offsets in the time series without influencing the velocity or reference frame terms. Only one equipment change was reported at a site on Oahu, which is not used in later analysis. Following estimation, we remove the average velocity of each site as well as the estimated reference frame errors. The residual time series are analyzed for slow slip events.

4. Identifying Slow Slip Events

4.1. Motivation

[16] The previously identified slow slip events on Kilauea are clearly visible as offsets in the GPS time series (e.g., Figures 2 and 4, map view) [*Cervelli et al.*, 2002; *Segall et al.*, 2006; *Brooks et al.*, 2006]. There may, however, be smaller events that are not easily visible in the data. Identifying additional events will help us determine fundamental properties of slow slip events, such as how often they occur, their size distribution, and if they are periodic or follow simple recurrence relations.

[17] The Kilauea slow slip events were initially identified on the basis of the spatial coherence of the GPS displacements for stations on the south flank, differentiating them from other events such as eruptions/intrusions, or reference frame errors. Reference frame errors are also spatially coherent but the coherence extends across the entire network [*Cervelli et al.*, 2002], not just the south flank stations. Intrusion induced deformations in Kilauea's rift zones show
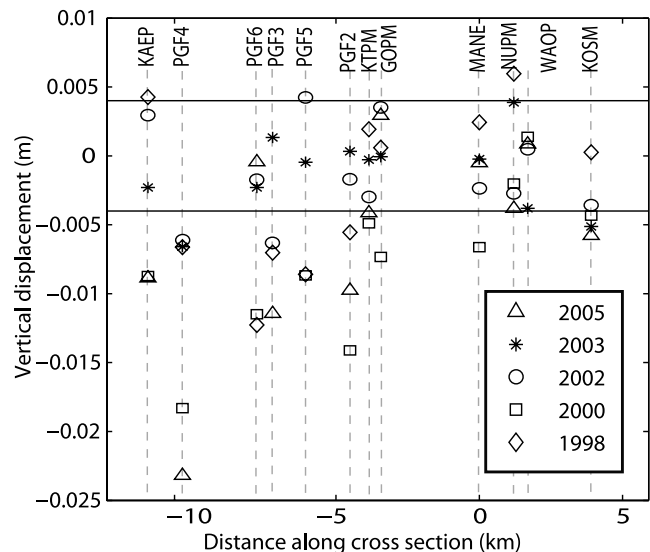

Figure 3. Vertical displacements for the previously identified slow slip events, defined in Table 1, showing a majority of stations subsided during the largest slow slip events. Horizontal lines show average standard deviations for vertical displacements on Kilauea computed for the longest uneventful period in the GPS time series (roughly the year 2001), and vertical dashed lines connect the displacement markers to station names. The rift perpendicular cross section is noted in Figure 16.
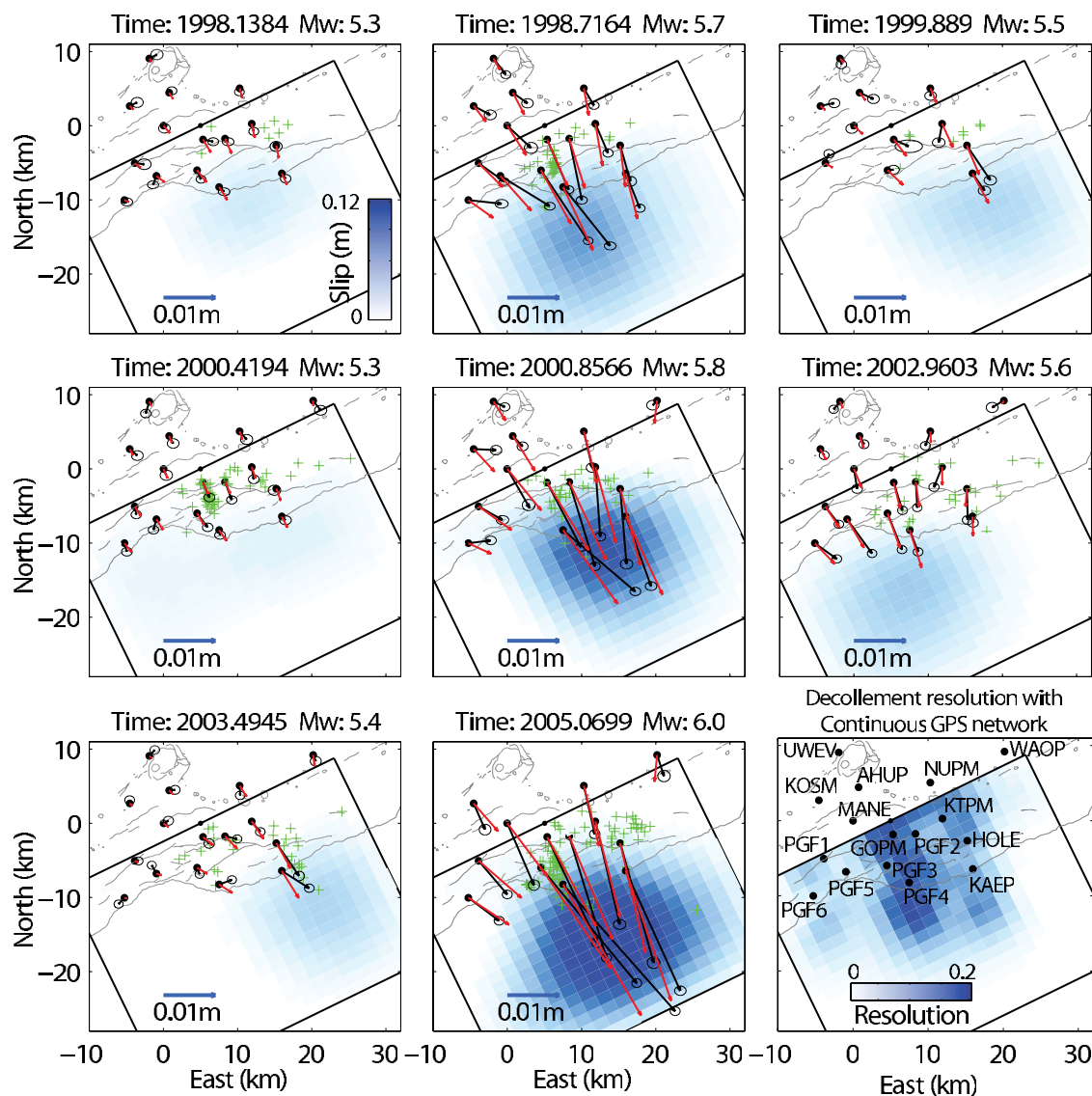
Figure 4. Displacements and slip distributions for the previously and newly identified slow slip events listed in Table 1. Displacements are computed from a 10-day window on either side of the event as in Figure 2. (black) Observed with 95% confidence ellipses; (red) Predicted from the indicated slip model. The decollement fault plane is constrained to a depth of 7.5 km, and Green's function's include layered elastic structure and a topographic correction. (bottom, right) The diagonal elements of the resolution matrix on the fault plane. The green crosses are the catalog earthquake locations from 1 day before to 10 days after each slow slip event.

extension localized across rift zones, resulting in northward motions of stations north of the rift. Slow slip events on the other hand do not show extension across either the rift zones or the summit, and in fact, stations north of the rift and summit move south (Figure 4, November 2000 and January 2005).

[18] Although they might be too small to see easily in the time series, there may be other events that have displacement fields similar to previously identified slow slip events. These events could be easily missed by visual inspection, but could be identified by an automated algorithm. Therefore, an automated method to search for events with similar displacement patterns is highly desirable. This method could easily be

expanded in the future to search for other types of events including magmatic events.

[19] In section 4.2, we develop an algorithm that can be used to search for slow slip events that may not be visible in the GPS time series. We attempt to find new, perhaps smaller, events by comparing the spatial patterns of displacements with those of previously identified events. This method assumes the events we seek produced displacement patterns similar to previous events and over similar time intervals (2 days).

4.2. Identification Procedure

[20] Before attempting to identify slow slip events, a standard method of computing the displacement offsets at
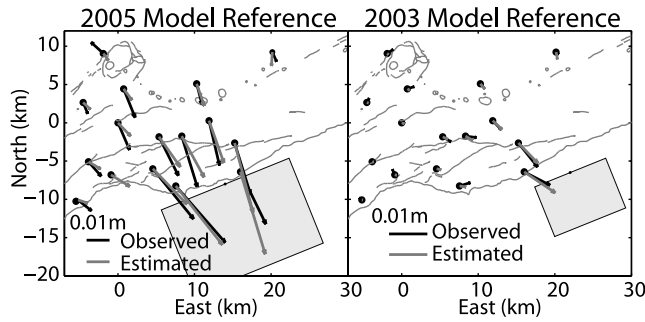
Figure 5. Map view of displacement fields due to the best fitting January 2005 and July 2003 single uniform slip dislocation. These displacement fields will be used as the reference event to compare with candidate slow slip events.

each GPS station must be defined and computed for each previously identified and each candidate slow slip event. Previously identified events lasted 36–48 h [*Cervelli et al.*, 2002; *Segall et al.*, 2006], and thus appear almost as offsets in the daily GPS time series.

[21] We determine displacements for each candidate event using a running mean of 10 days on either side of a 3-day window surrounding the candidate day. The 3-day window is longer than the duration of the well-studied Kilauea slow slip events in 2000 [*Cervelli et al.*, 2002] and 2005 [*Segall et al.*, 2006]. Since the steady-state velocity was removed from the entire time series, we compute the displacement from a 23-day window of data ($d_{i-11:i-1}$ to $d_{i+1:i+11}$) at each candidate time as

$$d(t_i) = d_o + \Delta d H(t_i), \qquad (2)$$

where $H(t_i)$ is a heaviside function at time t_i, and d_o is an initial position at the beginning of the current time window.

[22] The reference displacements, to which we compare candidate slow slip events, are computed from the single uniform slip dislocation model that best fits the displacements observed from 2005 slow slip event (discussed below). The reference event displacements exhibit the main characteristics of many of the slow slip events on Kilauea (Figure 5, left). The largest displacements are in the southeast at the coastal sites (KAEP and PGF4) and decrease to the north and west. Because of recently active lava flows, there are no GPS sites east of KAEP near the coast.

[23] The displacements determined from a similar uniform slip model of the 2003 slow slip event will also be tested as a reference because this event has different displacements from the other previously identified events, and occurred mainly in the eastern part of the network [*Brooks et al.*, 2006; *Segall et al.*, 2006]. We use the computed displacements as a reference, rather than the observed displacement field because we want to avoid matching the noise that dominates the observed displacements at far-field GPS sites. We also tested a stack of the four largest previously identified slow slip events, which had similar features to the 2005 modeled displacements, but the far-field sites were again randomly oriented. Because we are specifically interested in finding small slow slip events, false detections can arise from matching small, but randomly oriented, observed far-field displacements. While not influencing matches to the 2005

slow slip event, the negative effects of matching the far-field noise are particularly prominent in the case of the 2003 slow slip event, for which the majority of the observed displacements occur at just three of the sixteen sites.

[24] As a measure of similarity, we take the projection of the 3N-dimensional candidate displacement vector onto the 3N-dimensional reference vector, where N is the number of stations available in each candidate displacement field. We put the three components (east, north, and up) of displacement at each site into a 3N-dimensional column vector,

$$\begin{bmatrix} E_1 & E_2 & \dots & E_N \\ N_1 & N_2 & \dots & N_N \\ U_1 & U_2 & \dots & U_N \end{bmatrix} \Rightarrow \qquad (3)$$

$$[E_1 \ N_1 \ U_1 \ E_2 \ N_2 \ U_2 \ \dots \ E_N \ N_N \ U_N]^T. \qquad (4)$$

The angle, θ, between the reference vector, Δd_{ref}, and each candidate displacement, Δd is determined from the dot product of the two vectors:

$$\cos(\theta(t)) = \frac{\Delta d_{ref} \bullet \Delta d(t)}{\| \Delta d_{ref} \| \| \Delta d(t) \|}, \qquad (5)$$

where $-\pi < \theta < 0$. When the candidate displacement field is similar to a slow slip event, the 3N-dimensional vectors are nearly parallel, resulting in an angle, θ, close to zero. The time series of angles, $\theta(t)$, is peaked at the times of the slow events, with the height of the peaks being a measure of the vectors' similarity, which is later converted to a probability. Note that $\theta(t)$ is independent of the magnitude of the displacement. Thus small amplitude events with the same spatial pattern of the reference can be detected.

[25] The Kilauea GPS network contains significantly more stations to the south of the rift zones than north. It is important to differentiate accelerated southward flank motion due to slow slip events from transient expansion in the rift zones. Both processes produce southward displacements in GPS stations south of the rift zones. To balance this effect, and increase our ability to discriminate between rift zone and flank events, we weight stations north of the rift zones and caldera five times heavier than the south flank stations. This roughly equalizes the sites north and south of the rift zones, which significantly, but not completely, inhibits false detections of intrusions as slow slip events.

4.3. Identification Results

[26] Candidate events that the algorithm identifies as similar to the reference event are indicated by a sharp peak at the time of the event with an angle, θ, close to zero. The algorithm shows strong peaks for the three largest previously identified events (Figure 7a), which occurred on 20 September 1998, 9 November 2000, and 26 January 2005.

[27] The candidate displacements are increasingly uncorrelated with the reference displacements for increasingly negative θ. The 2005 event is most similar, with $\theta = -0.52$ radians (Figure 7). This is expected since the reference displacements are computed from a model of this event. The remaining four previously identified events (Table 1) are also very similar with angles ranging from $\theta = -0.54$ to $\theta = -1.00$ radians. The 2003 event has a much larger angle
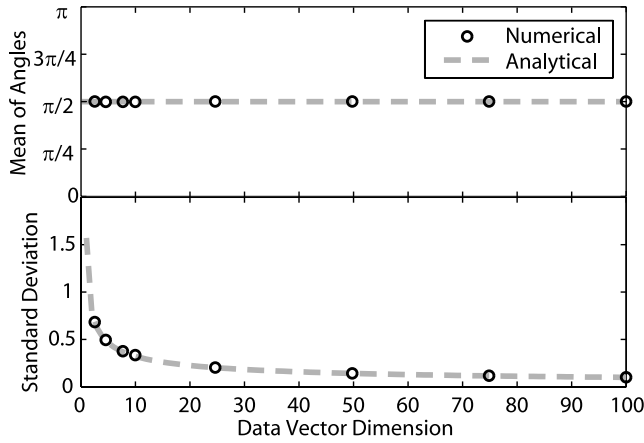
Figure 6. (top) Mean and (bottom) standard deviations of the angles between a reference and 10,000 randomly generated candidate vectors of varying dimensions. As the number of available data points ($3N$, where N is the number of GPS stations) increases, the standard deviation of the angle between the vectors decreases as $1/\sqrt{3N}$ (dashed), while the mean remains at $\pm\pi/2$.

($\theta = -1.25$) consistent with its different displacement pattern. We will discuss the 2003 event in more depth later in this section when we use it as a reference event to look for other similar slow slip events.

[28] Smaller, yet still prominent, peaks highlight the need for setting criteria for distinguishing new slow slip events from random noise. We start with the top 95th percentile of the angles between the reference and candidate displacements (Figure 7c) to provide a short list of events that we subjected to additional manual inspection. The next few paragraphs discuss both theoretical and numerical methods for determining an optimal threshold.

[29] To determine a theoretical mean and variance of the distribution of angles (θ, equation (5)), we start by assuming normally distributed noise at each GPS station. Choosing a coordinate basis that is parallel to the reference vector, such that the unit reference vector has only one nonzero element equal to 1, say Δd_{1ref}, then equation (5) becomes

$$\cos(\theta) = \Delta d_{1ref} \frac{\Delta d_1}{\| \mathbf{\Delta d}\|} = \frac{\Delta d_1}{\| \mathbf{\Delta d} \|} \qquad (6)$$

since $\Delta d_{1ref} = 1$. If the elements of Δd are randomly distributed, then as the dimension of the vector Δd increases, the ratio $\frac{\Delta d_1}{\|\Delta d\|}$ approaches zero, so that the expected value of $\cos(\theta)$ is $-\frac{\pi}{2}$ on the interval $[-\pi, 0]$. The variance of this distribution can be derived from the density of a multivariate normal distribution, which is constant over multidimensional ellipsoids [*Anderson*, 2003]. Normalizing the vectors produces a uniform distribution over a multidimensional unit "spheroid," which has a variance of $\sigma^2 = 1/(D)$, where D is the dimension ($3N$). Thus, the variance of the computed angles is

$$\sigma_\theta = 1/\sqrt{3N} \qquad (7)$$

[*Anderson*, 2003]. For numerical comparison, the angles between randomly generated multidimensional vectors were

generated, and the mean and standard deviations of the resulting angles were computed (Figure 6).

[30] The top 2σ boundary based on this standard deviation is $\theta = -1.28$ assuming the average number of station components available ($3N = 45$). The observed 2σ bound, however, is $\theta = -1.00$ suggesting that the observed distribution is influenced both by the presence of real events, and nonnormality of the errors. The lower 2σ bound, which should be free of slow slip events, is also wider ($\theta = -1.99$) than predicted by the normal distribution ($\theta = -1.84$), so the theoretical bounds do not adequately define a threshold.

[31] In another approach, we can convert the computed angles into a probability, p, that a candidate event is a slow slip event by using the method of *Hooper et al.* [2007]. This method determines the probability density of an unknown population from one known population, the observed data, and a second modeled population of random occurrences. If we assume that the observed density of the angles, $p_{obs}(\theta)$, is the sum of the probability densities for a set of random occurrences, $p_r(\theta)$, and the set of slow slip events $p_{ss}(\theta)$, then the observed probability density can be written as

$$p_{obs}(\theta) = \alpha p_{ss}(\theta) + (1 - \alpha)p_r(\theta), \qquad (8)$$

where $0 \le \alpha \le 1$. For observed angles $\theta < -\pi/2$, the probability of being a slow slip event is small, $p_{ss} (\theta < -\pi/2) \approx 0$. We approximate p_r as a Gaussian fit to the observed angles $\theta < -\pi/2$. These probability distributions are presented in Figure 9. Within this interval, the observed and random distributions should be proportional, and we estimate a conservative value of α as

$$\int_{-\pi}^{-\pi/2} p_{obs}(\theta)d\theta = (1 - \alpha) \int_{-\pi}^{-\pi/2} p_r(\theta)d\theta. \qquad (9)$$

The probability, then, that the value of θ indicates a match to the reference event is

$$P(\theta \in ss) = 1 - \frac{(1 - \alpha)p_r(\theta)}{p_{obs}(\theta)} \qquad (10)$$

As with the InSAR persistent scatterers studied by *Hooper et al.* [2007], the observations are not monotonically decreasing because of the presence of noise, so they are smoothed with a 9 point Gaussian window. The probability of each candidate event being a slow slip event is listed in Table 1.

[32] After computing theoretical thresholds, and corresponding probabilities, we would like to compare these values to distributions derived from the observed data. To determine the distribution of angles that would arise by random chance, we generate 1000 random reference displacement fields and compare them to each candidate displacement. Figure 8a shows an example random displacement field (Figure 8a) and the angles between this random reference and each candidate in the data set (Figure 8b). No candidate days are as similar to this random reference as several candidates are to the reference on the basis of the 2005 slow slip event. For the entire set of 1000 random vectors, the mean angle is -1.57 ($-\pi/2$) and the upper 2σ bound is $\theta = -1.29$ (Figure 10), equivalent to the theoretical bound
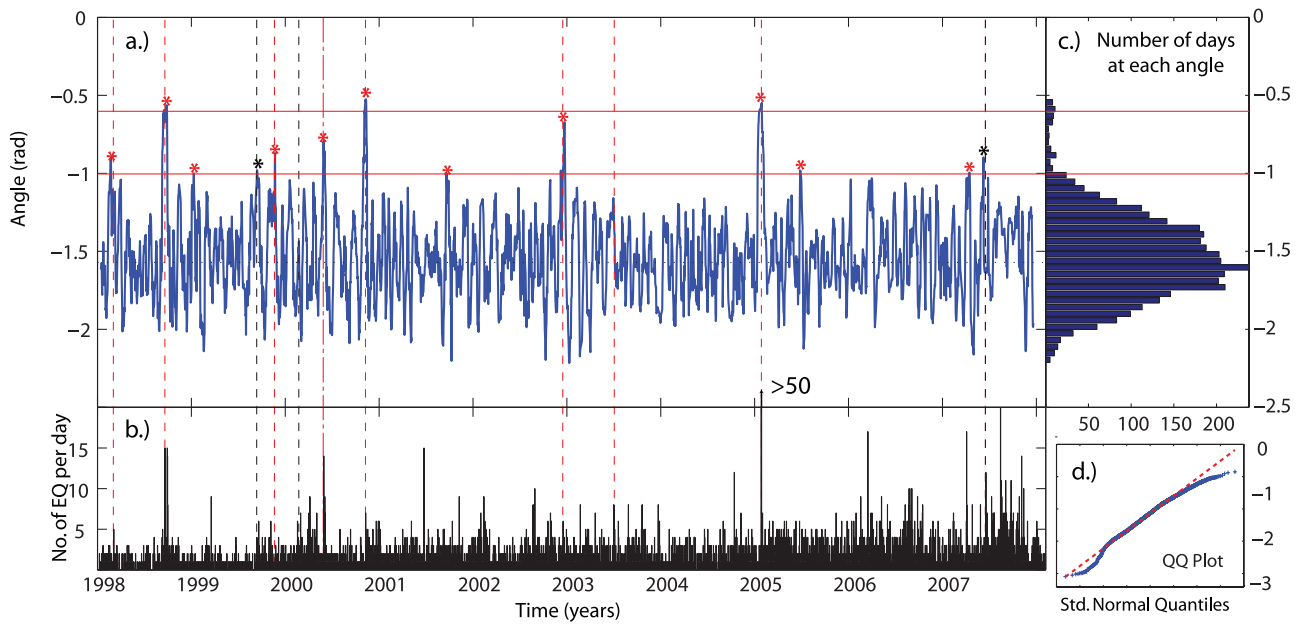
Figure 7. (a) The angles between the reference 2005 event and each candidate data vector. Angles are defined on the range $-\pi \le \theta \le 0$, so peaks indicate high correlation with the reference event. Candidates with peaks close to zero show highly similar displacement patterns to the reference. Solid horizontal red lines indicate the top 95th and 99th percentile of the histogram in Figure 7c. Red vertical dashed lines show the times of events that have been previously identified in Table 1, and black vertical dashed lines show the times of rift zone intrusions. Red stars indicate candidates that exceed the 95th percentile; black stars exceed the 95th percentile, but are known intrusions. (b) Histogram of catalog earthquake counts from the south flank in daily bins. (c) A histogram of all angles computed in Figure 7a. (d) QQ-plot of the quantiles of data (angles) versus quantiles of a standard normal distribution.
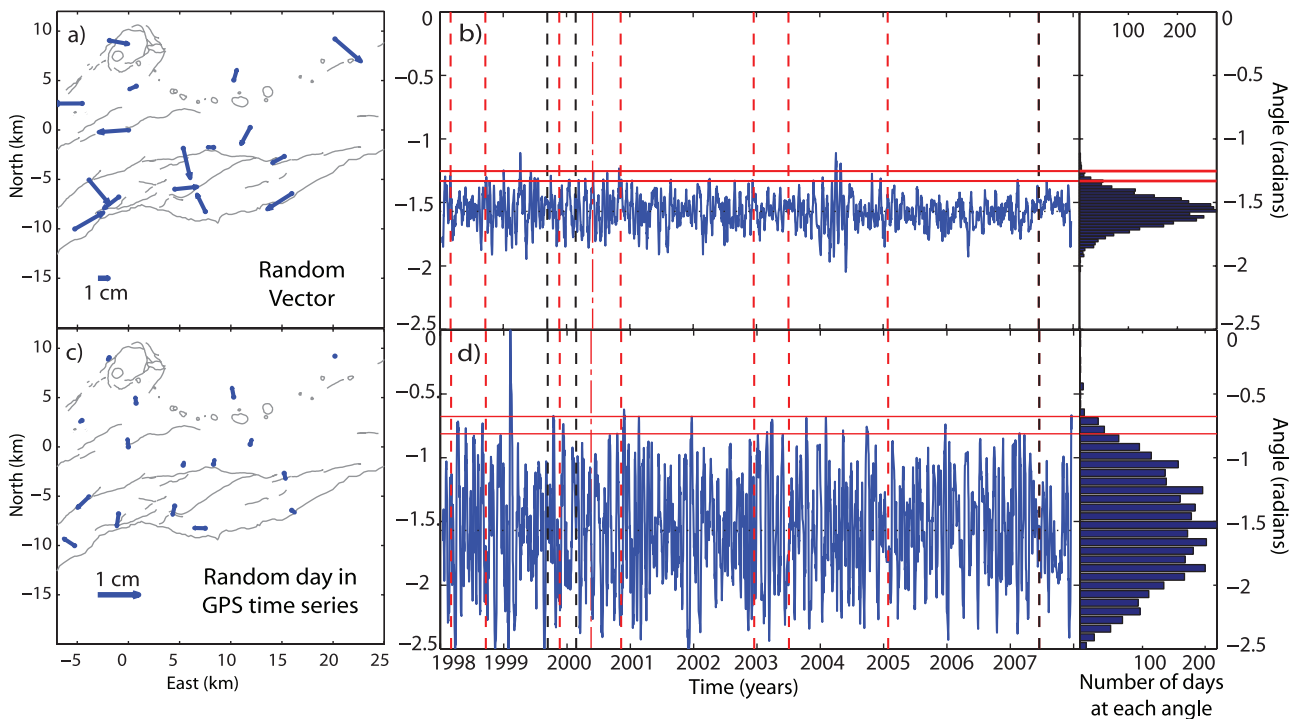

Figure 8. (a) Map view of the example displacement field from a random vector. (b) Angles relative to the example random vector. (c) Map view of the example displacement field from a worst case random day in the GPS time series. (d) Angles relative to the example random day. Indicator lines are the same as Figure 7.
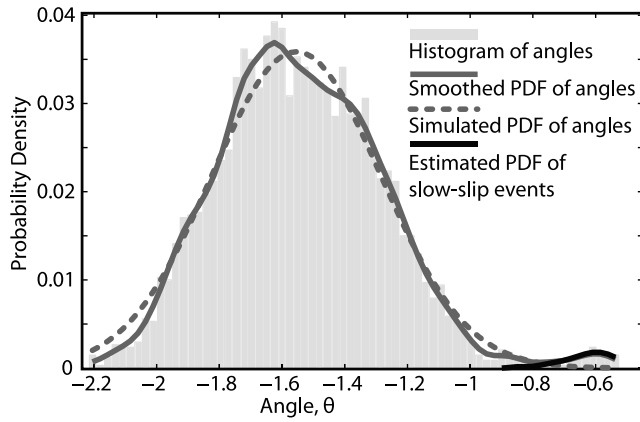
Figure 9. Observed probability density for the distribution of angles, shown in dark gray, for the full range of observed angles. The probability density of random angles, simulated as a Gaussian distribution with mean $\pi/2$ and standard deviation of $1/\sqrt{3N}$ (dashed). The probability density of slow slip events is shown in black.

(equation (7)). We repeated this test using 1000 of the candidate days as random references (a broadly distributed worst case example is shown in Figure 8c), rather than simply random vectors, and find similarly that the distribution of angles has a mean of −1.56, but upper 2σ bound of −0.71 (Figure 10). A Q-Q plot of the random day angles show that they are not strictly normally distributed, which the theoretical mean and standard deviation computations assume.

[33] The theoretical 2σ bound computed in equation (7) is $\theta = -1.28$, assuming an average number of available station components ($3N = 45$). This variance is consistent with the 2σ bound of −1.29 from the distribution of angles computed from the 1000 randomly generated vectors, but not from the 1000 random days, indicating that the observed data are not independent (i.e., despite having removed a secular velocity, the stations are still much more likely to move southward than north). This leads us to believe that the probability estimated by equation (10) provides a more realistic threshold than the previously discussed theoretical bound (equation (7), $\sigma = 1/\sqrt{3N}$).

[34] The spatial patterns of the slow slip displacements (Figure 4) are similar to the average steady-state velocities on Kilauea (Figure 1). The angle between the $3N$-dimensional vectors for the average velocities and the 2005 slow slip reference is $\theta = -0.91$, while for the 2003 slow slip reference, $\theta = -2.0$. These angles correspond to a probability of being a slow slip event of 60% and nearly zero, respectively. Therefore, slow slip events similar to the 2003 reference have very little chance of being confused with other background motions that may be temporally nonlinear, while slow slip events similar to the 2005 reference may. Typical steady-state displacement rates at coastal stations of up to 7 cm a^{-1} are much slower than slow slip velocities at the same sites of 350 cm a^{-1} (1 cm d^{-1}) and require steady-state displacements to speed up by 50 times to reach slow slip velocities.

[35] Candidate events with angles close to π also exist (Figure 7), which would seem to indicate that they are similar to the reference, but moving in the opposite direction. The candidates with angles close to π are in fact slight decreases in displacement rate relative to the steady-state velocity that

was removed from the time series, and therefore appear as slight landward displacements in the detrended GPS time series.

[36] The 10-day averaging windows used to compute the displacements for each candidate limit the time resolution of the inferred slow slip events. In these cases, the candidate day with the largest vector norm $|\Delta d|$ of the $3N$-dimensional vector is chosen. Because the detected events are not exactly the same as the 2005 event, perhaps because of somewhat different source location or unresolvable slip migration, the minimum θ (maximum similarity) is not always the day with the largest displacements (maximum $|\Delta d|$). For most candidate days with greater than 50% probability of being a slow slip event, the largest vector norm is on the day with the angle closest to zero; the rest are either the day before or the day after.

[37] We compute additional attributes of candidate events in the top 95th percentile including their magnitudes (the total amount of slip, integrated over the fault area, estimated in section 5) and number of coshocks and aftershocks. Since the larger previously identified events were all accompanied by heightened levels of microseismicity, we quantify the change in seismicity rate for each candidate by computing the ratio of the number of earthquakes 3 days after to 3 days before all potential slow slip events (Table 1). The microearthquakes are located in the box bounded by longitude −155.2551 and
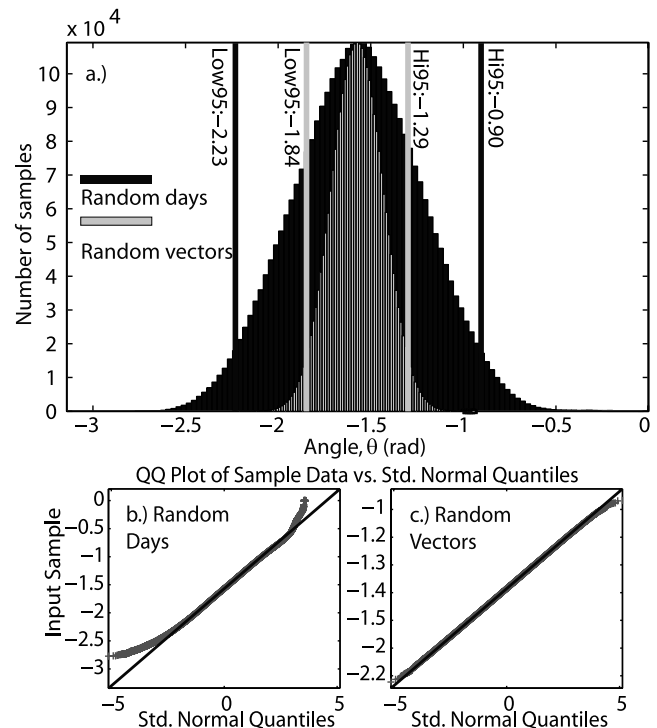

Figure 10. (a) Histograms of all angles between each candidate and 1000 random vectors and 1000 random candidates. Vertical lines indicate the 2σ bounds of the distribution. Note that the 2σ bounds for the random vectors (gray) are more consistent with the theoretical variance based on the number of stations available, while the 2σ bounds for the random days (black) have a much greater variance. (b and c) QQ-Plots of the distribution of angles from random day and random vectors.
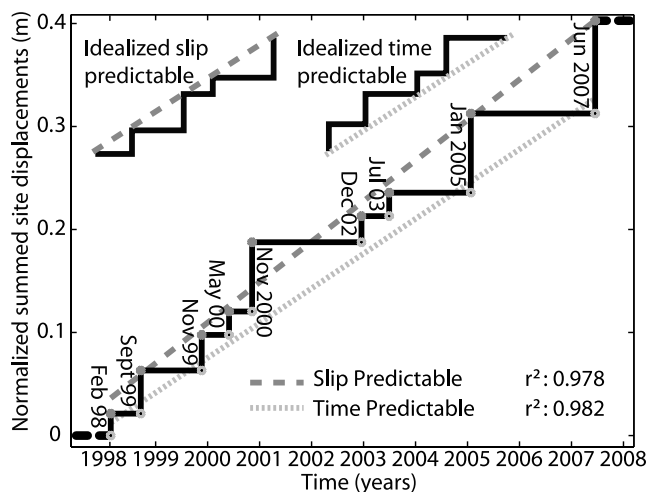
Figure 11. Comparison of time predictable and slip predictable models for the recurrence of Kilauea slow slip events. Neither a time-predictable nor slip-predictable, nor a purely periodic model appears to apply to the whole sequence of slow slip events on Kilauea.

−155.0296 and latitudes 19.2264 and 19.3538 (on the map: east between 2 km and 25.5 km, and north between −12.5 km and 1.5 km). A ratio greater than one indicates an increase in seismicity following the slow slip event and less than one indicates a decrease.

[38] Since the potential new events are all very small, the increase in seismicity may not be as intense as observed for the previously identified larger events. The day after the 2005 slow slip event had >50 earthquakes in an area that typically experiences an average of 1.6 earthquakes per day, resulting in a ratio (after/before) of 10.5. The remaining previously identified events produced 10 earthquakes per day, with seismicity ratios of 2−4. Although the previously identified slow slip events coincide with heightened seismicity, not all potential new slow slip events coincide with increased seismic activity. Additionally, as can be seen from Figure 7b, not all swarms of microseismicity coincide with potential new slow slip events as identified by the similarity of their displacement fields. In fact, 90 days in the study period had >5 earthquakes, however only six of those days correlate with slow slip events.

[39] Five potential new slow slip events are identified as similar to 2005 slow slip event, beyond those previously identified (Table 1). The potential slow slip event with the highest probability of being a slow slip event (75%) and the second largest overall earthquake ratio, occurred on 29 May 2000, 2 months after a M5.0 South Flank earthquake on 2 April 2000 [*Miklius et al.*, 2005]. This earthquake's epicenter was midway between the bend in the East Rift Zone and the Hilina Pali. Because the candidate displacement fields are computed with a 10-day trailing window, the 29 May 2000 slow slip displacements are likely not influenced by the M5.0 earthquake; aftershocks from the M5.0 earthquake had also subsided by this time. The similarity in displacement fields, the elevated microseismicity ratio, and the lack of other magmatic or tectonic events at this time provides compelling evidence for a slow slip event on 29 May 2000.

[40] The remaining four potential slow slip events have less similar displacement fields to the 2005 reference event with angles of $\theta = -0.98$ to $\theta = -1.00$ corresponding to a 55−56% probability of being a slow slip event. Although these events are in the top 95th percentile, they correlate less well with the 2005 reference event than the average velocities (Figure 1) for which $\theta = -0.91$. They are also not associated with significant increases in seismicity, with ratios ranging from $0.7 - 1.36$. The most recent possible new slow slip event in Table 1, 16 April 2007 is intriguing because it occurs close to the 2.11 ± 0.01 year recurrence time of *Brooks et al.* [2006] following the large January 2005 slow slip event. It was also preceded by several tectonic events that produced seismic signals on Kilauea including a teleseism from the M8.0 Solomon Islands earthquake which arrived midmorning on 2 April 2007. The teleseism was followed within a day by a shallow (<5 km) swarm of 30 microearthquakes (M < 3) under Apua Point lasting from 3 to 6 April. Between the seismic swarm and the potential slow slip event was a deflation-inflation magmatic event at the summit from 5−10 April 2007. The remaining three potential events (10 January 1999, 19 September 2001, and 27 June 2005), have a low probability of matching the 2005 slow slip event, are very small and do not have any additional distinguishing features.

[41] Although most of the previously identified slow slip events appear to have very similar displacement patterns, there is at least one previously identified event (July 2003) that has a distinctly different pattern. The 2005 reference displacements (Figure 5) showed significant displacements at all stations on and south of the Palis. However, the July 2003 event shows more deformation localized to the eastern part of the network with maximum displacements at KAEP (Figure 5, right). Using the same method with this event as the reference we test whether there are additional slow slip events of this type. Again, because of active lava flows, there are no GPS sites in the immediate area east of KAEP. The localized nature of the 2003 event means that most of the stations in the western part of the network have nearly zero
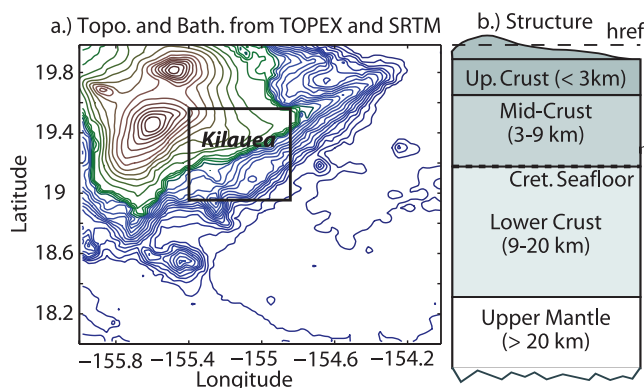

Figure 12. (a) Combined topography and bathymetry used for topographic correction. Topography data were combined from TOPEX and SRTM data. (b) Layered elastic structure used to approximate the effects of differing elastic properties of the upper crust, midcrust, lower crust (below the old Cretaceous sea floor), and upper mantle.
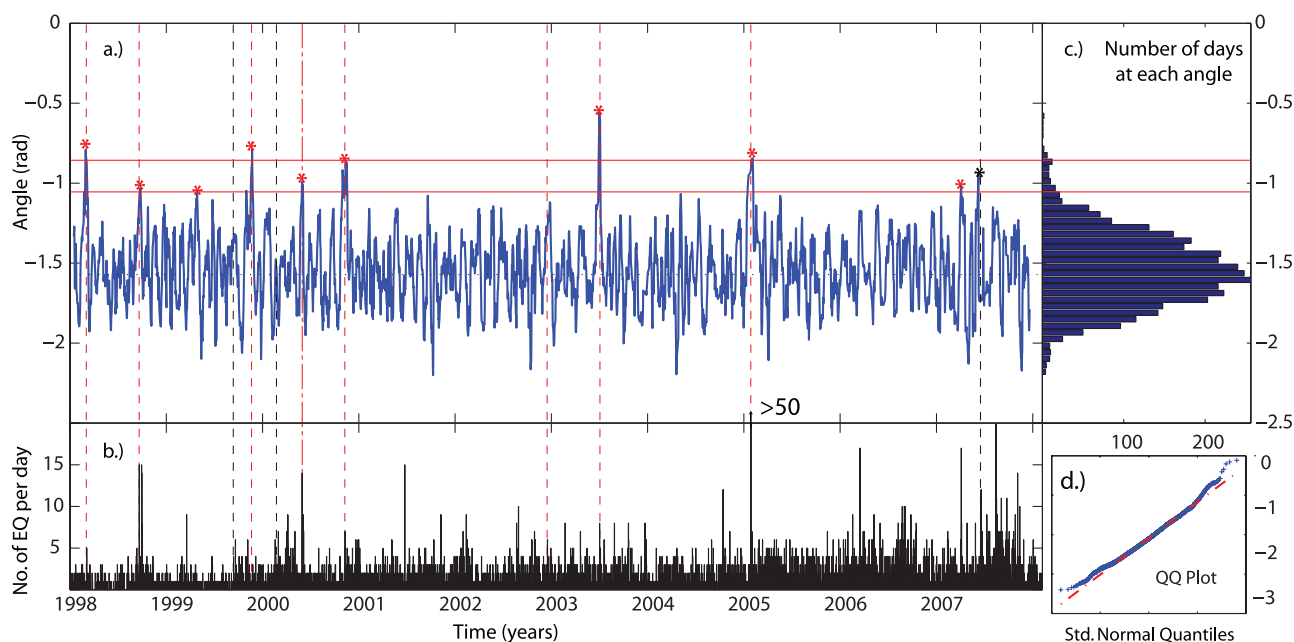
Figure 13. (a) The angles between the reference based on the 2003 event and each candidate data vector. Candidates with peaks close to zero show highly similar displacement patterns to the reference. Solid horizontal red lines indicate the top 95th and 99th percentile of the histogram. Red vertical dashed lines show the times of events that have been previously identified in publications, and black vertical dashed lines show the times of rift zone intrusions for reference. Red stars indicate candidates that exceed the 95th percentile; black stars are in the 95th percentile, but are known intrusions. (b) Histogram of catalog seismicity counts from the south flank in daily bins. (c) A histogram of all angles computed. (d) QQ-plot of the quantiles of data (angles) versus quantiles of a standard normal distribution.

displacements, and their directions then are presumably dominated by noise. A consequence of this that the similarity between the observed 2003 displacements and those computed from the slip model is significantly weaker than the similarity between the observed 2005 event and its model despite the same quality of model fit.

[42] Ten candidate events are indicated as possible slow slip events by the 2003 reference, however, most are duplicated from those that match the 2005 reference; two additional potential events are uniquely identified by the 2003 reference (Figure 13). Both events are small and have much less similar displacement fields with angles of $\theta = -1.06$. The 27 April 1999 candidate has an earthquake ratio of 0.37, while the earthquake ratio for the 6 May 2004 candidate is 1.7. Although these angles correspond to a 70% chance of being a slow slip event given the distribution of candidates similar to the 2003 event, neither is large enough, or accompanied by significant coshocks and aftershocks, to make a compelling case.

[43] The four events that have the strongest similarity to the 2005 slow slip event (20 September 1998, 9 November 2000, 16 December 2002, and 25 January 2005; all previously identified events), appear to be somewhat periodic. They are each separated by approximately 2.11 ± 0.01 years (Figure 7) [*Brooks et al.*, 2006]. Overall, however, the detected events do not exhibit periodic behavior. Including all events with probability of over 75%, the mean recurrence time is 0.94 years with a standard deviation of 0.61 years. The whole sequence also appears to be neither time-predictable

[*Shimazaki and Nakata*, 1980] nor slip-predictable [*Bufe et al.*, 1977] (Figure 11).

5. Slow Slip Source Location and Geometry

[44] The next step in understanding the Kilauea slow slip events is to accurately determine the locations of the slow slip source. A Monte Carlo method [*Metropolis et al.*, 1953] is used to find the distribution of fault-source parameters assuming a uniform slip dislocation in a homogeneous isotropic elastic half-space for the 2005 slow slip event. *Cervelli et al.* [2002] assumed a half-space model and found that the November 2000 event likely occurred on a shallow dipping thrust fault at a depth of 4.7 km. However, on the basis of the results of *Segall et al.* [2006], we believe a deeper source may be more realistic. *Segall et al.* [2006] showed that the 2005 slow slip event was accompanied by coshocks and aftershocks located at depths between 6.5–8.5 km. Assuming *Dieterich*'s [1994] seismicity rate theory applies, they also showed that the temporal evolution of earthquakes was consistent with the static stress change due to the slow slip. Despite shallower half-space source results, depths of 6.5–8.5 km are more consistent with the locations of the triggered seismicity. Slip models constrained to these depths fit the 2005 GPS data nearly as well as shallower models, highlighting a lack of depth resolution in the GPS data.

[45] In this section, we test whether the optimal geodetic depth can be reconciled with the aftershock locations by including the effects of both topography and a layered elastic structure in the forward models. We explore four different

forward models: uniform elastic half-space, layered elastic half-space, uniform elastic structure with topographic correction, and layered elastic with topographic correction.

5.1. Topography

[46] The subdued topographic slopes of shield volcanoes, such as Kilauea, might suggest that topographic variations do not significantly influence the deformation field, leading most researchers to focus on elastic half-space models. However, many researchers using perturbation methods, or boundary and finite element models, have found that even modest topographic variations can influence the deformation field [*McTigue and Segall*, 1988; *Cayol and Cornet*, 1998; *Williams and Wadge*, 1998]. *Cayol and Cornet* [1998] found that average slopes of a volcano's flanks exceeding 20% can lead to a 15–20% miscalculation of the change in volume of a Mogi source in a half-space. *McTigue and Segall* [1988] found that characteristic slopes of $10–20^{\circ}$ could produce corrections as large as 20–40% in two-dimensional models. Average slopes on Kilauea are about 10°, but maximum slopes can be as much as 20% onshore and 40% immediately offshore on the basis of combined digital elevation models (DEM) and bathymetry. Consequently, the source parameters estimated by inversion can be significantly altered.

[47] We explore whether topography on the south flank of Kilauea is sufficient to influence the optimal depth of the slow slip sources. The topographic model used (Figure 12a) combines a surface DEM from SRTM (http://www2.jpl.nasa.gov/srtm/dataprod.htm) with bathymetry from TOPEX (http://topex.ucsd.edu/marineopo) [*Yun et al.*, 2005].

[48] We use the method of *Williams and Wadge* [2000] which provides a quasi-analytical technique for including topographic effects of small slope. The topographic correction is the sum of two terms; the first is the product of topography and the vertical derivatives of the zero-order (half-space) solution. The second term is a function of stresses from the zero-order (half-space) solution and Green's functions from an elastic half-space. All of these terms are known or can be computed from the half-space solution and topography. The topographic correction must be computed over an area far beyond the extent of the network to avoid edge effects.

5.2. Heterogeneous Elastic Structure

[49] Most volcano deformation models are computed in a homogeneous elastic half-space [e.g., *Okada*, 1985; *Mogi*, 1958]. However, the structure under Kilauea is a composite of the volcanic pile and the oceanic crust below. We assume a plane-layered model in which the shear modulus for each layer is estimated from the s-velocity and the density ($\mu = V_s^2\rho$). V_s is determined from the average p-velocity and V_p/V_s ratio tomography results of *Hansen et al.* [2004]. Estimated densities in the top layer are consistent with those found in cores from the Hilo drill hole ranging from 2.0–3.1 g cc^{-1} between 889 and 3097 m below the surface [*Moore*, 2001], and increase slightly with depth. *Hill and Zucca* [1987] report densities of 2.9 g cc^{-1} for the lower crust, and 3.25 g cc^{-1} for the upper mantle off the coast of Kilauea on the basis of combined onshore Bouguer gravity and offshore free-air gravity data. We approximate the structure of Kilauea with four layers including shallow volcanic crust (0–3 km, $\mu = 24\,GPa$), volcanic midcrust (3–9 km, $\mu = 40\,GPa$), Cretaceous

sea floor (9–20 km, $\mu = 60\,GPa$), and upper mantle (>20 km, $\mu = 80\,GPa$) (Figure 12b). Poisson's ratio (v) is 0.25 for all layers.

[50] We use the propagator matrix method [*Segall*, 2009], which provides an analytical solution for a vertically stratified elastic half-space. In the implementation of the propagator matrix method, the solution for a point source in a layered elastic media is computed and the finite dislocation is achieved by numerically integrating the sources using Gauss quadrature.

5.3. Effects of Topography and Layering

[51] While a rigorous approach would be to compute the topographic corrections by perturbing the flat multilayered solution, this approach would require computing the surface parallel stresses and the Green's functions in the layered media. Instead, we use a simpler approach. Solutions including the topographic corrections and layered elastic structure are combined by computing the zero-order solution from the layered elastic Green's functions and applying topographic corrections computed from the homogeneous half-space solutions.

[52] The four different structural (forward) models produce similar distributions of source parameters, except for source depth. We compare the posterior distributions of accepted model depths for the 2005 event from each of the four forward models in Figure 14. Note that the uniform half-space model favors depths that are too shallow to coincide with the depths of the coshocks and aftershocks. Both the topographic correction and layered elastic structure deepen the depth distribution by a small amount, and the combination of the two puts the 2005 slow slip event at depths consistent with those of its coshocks and aftershocks [*Segall et al.*, 2006]. This analysis suggests that the slow slip and the coshocks and aftershocks occurred on the same fault structure.

[53] To obtain a distributed slip model for the slow slip events, we extend the best fitting uniform slip plane in length and width, and linearly invert for distributed dip slip on the decollement surface including the effects of topography and layered elastic structure in the Green's functions. We apply a Laplacian smoothing operator and a nonnegativity constraint requiring that all slip be seaward. Smoothing weights are determined by the L-curve criteria [*Hansen*, 1992] in which various values of the smoothing weights are tested (Figure 15). Increased smoothing decreases the model roughness, which is defined as the norm of the product of the smoothing operator and the slip model. The optimal smoothing weight is chosen when the weighted residual norm begins to increase rapidly relative to the model norm.

[54] Although the resolution of offshore slip is limited (Figure 4), we can see that the pattern of deformation is very similar from event to event, except for the 2003 event, which has slip concentrated to the east of the GPS network (Figure 4). This indicates for the most part that each of these events slip the same fault plane over and over again.

[55] Slow slip events and the steady-state sliding on Kilauea's south flank are both likely driven by seaward gravitational spreading [*Delaney et al.*, 1998] and/or deep rift opening [*Swanson et al.*, 1976] with slip accommodated at the interface of the volcanic pile with Cretaceous sea floor. Steady-state velocities at sites across nearly the whole south
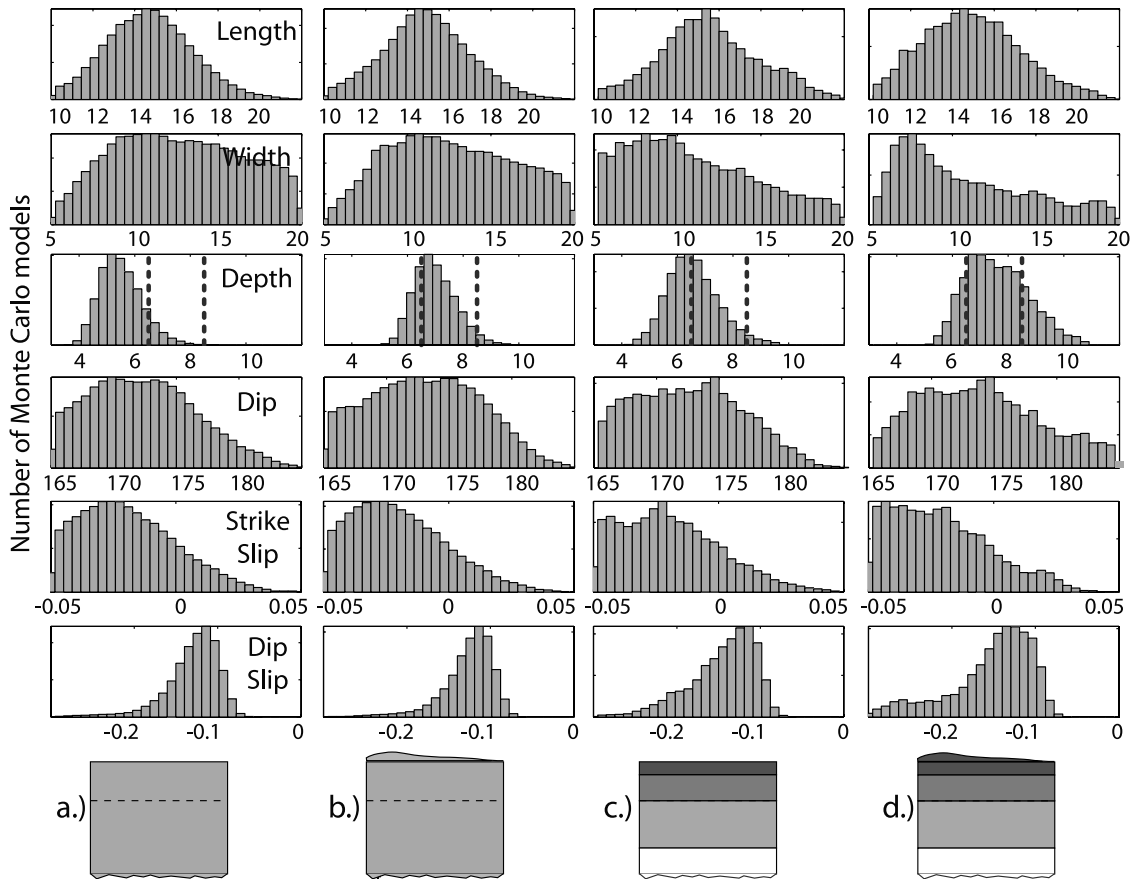
Figure 14. Posterior probability distributions for different uniform slip forward models of the 2005 slow slip event. Prior probability distributions are uniform with bounds indicated by the horizontal axis limits. (a−d) The schematic diagrams below each column indicate the model structure used. The parallel dashed lines on the depth plots indicate the depth range of the relocated accompanying seismicity (Figure 16). Note that addition of elastic structure and a topographic correction provide consistency between the location of the 2005 slow slip event and the depth range of 2005 slow slip event's aftershocks.

flank from 1990–1996 consistently displace to the south-southeast [*Owen et al.*, 2000a], while the slow slip event displacements localize to a much smaller area just offshore south of the Palis. The locations of slow slip event models are coincident with a seaward extension of the slip model of *Owen et al.*'s [2000a] steady-state deformation between 1990–1996, but no slow slip events are detected in the far western part to the south and west of the central caldera (Figure 16).

[56] The maximum slip during the 2000 and 2005 slow slip events is as much as 0.1 m. The other, smaller events had between 0.05–0.1 m of slip. *Owen et al.* [2000a] estimated about 0.28 m per year of steady slip on the decollement using a uniform elastic half-space model. Assuming a roughly 2-year repeat time, the slow slip events thus do not accumulate enough slip to account for the entire steady-state slip budget in that area, although there is a trade off between the amount of slip and the size of the area that slipped.

[57] Additionally, the decollement under Kilauea is known for producing large tsunami-genic earthquakes like the M7.2 1975 Kalapana earthquake [*Ando*, 1979; *Furumoto and Kovach*, 1979; *Lipman et al.*, 1985]. Slip distributions from geodetic observations of the Kalapana earthquake, recently reanalyzed by *Owen and Burgmann* [2006], indicate
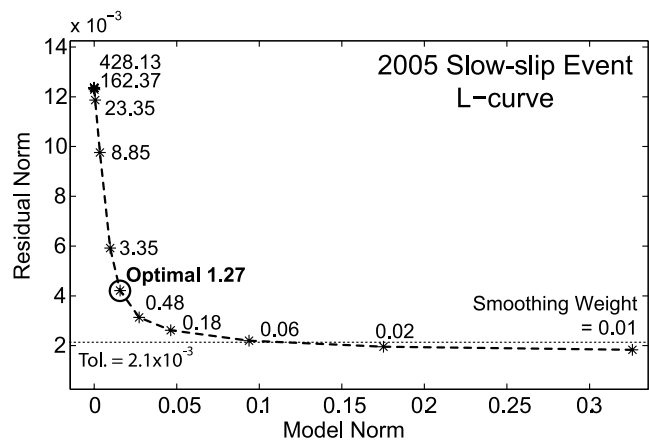

Figure 15. L-curve showing weighted residual norm ($\|(r^T \Sigma^{-1} r)/(N - M)\|$), a measure of data misfit versus model norm ($\|L\hat{m}\|$), a measure of model roughness, where L is a discrete Laplacian operator, for varying values of the smoothing weight. The optimal smoothing weight is chosen as the smoothest model with minimal increase in misfit.
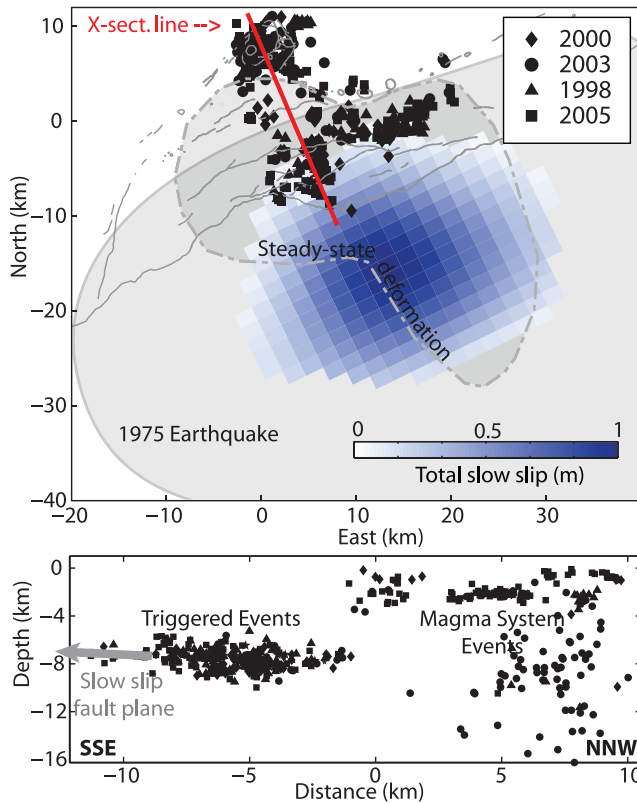
Figure 16. (top) Map view of relocated earthquakes with the cumulative slip distribution compared to the schematic locations of slip from the 1975 Kalapana earthquake [*Owen and Burgmann*, 2006] and steady-state deformation [*Owen et al.*, 2000a]. (bottom) Cross section of relocated earthquakes (NNW-SSE) parallel to the slow slip direction. Earthquakes are plotted for each of the five largest slow slip events from the start of the event to 10 days after.

that the highest amounts of slip occurred in similar locations as the slow slip events. However, slip extended 30 km offshore during the earthquake whereas the slow slip appears to be limited to 10 km offshore. Aftershocks of the 1975 Kalapana earthquake were also confined to the zone between the rift zone and the Palis [*Klein et al.*, 1987]. The ability of a single structure to host differing types of events like slow slip and regular earthquakes suggests highly variable physical properties on the fault surface.

[58] The limited offshore resolution on Kilauea brings into question how much of the offshore slip is required by the data. We test this by successively limiting the offshore extent of the fault by increments of 1.5 km. When offshore slip is not allowed, the large displacements at coastal GPS sites cannot be fit. If slip is constrained to be entirely offshore, all displacements are significantly underpredicted. Reasonable fits can be obtained when slip extends at least 15–20 km offshore, which is consistent with the seaward extent of the Hilina slump [*Morgan and McGovern*, 2003].

[59] We also test whether slip can be constrained to areas south of the large offset normal faults (Palis). Limiting slip to an area south of the Hilina Pali produces nearly equal misfits to models that allow slip on the whole rectangular fault. Limiting the slip to an area south of the smaller Holei Pali, however, is unable to fit the displacements at western flank

sites (PGF1, PGF5, PGF6). Slip appears to be unconstrained by Holei Pali, although, Hilina Pali may influence where slow slip occurs.

6. Time-Dependent Geodetic Inversion

[60] Daily solutions from GPS data are far too coarse to study the time evolution of the Kilauea slow slip events, which last only about 2 days [*Cervelli et al.*, 2002; *Segall et al.*, 2006]. There are many ways to obtain finer temporal resolution using kinematic GPS processing. We employ the Kalman filter method of *Cervelli et al.* [2002] which uses the spatial coherence of displacements due to fault slip to minimize the impact of multipath and other spatially incoherent noise sources. This approach requires estimation of just one scalar slip instead of independent station positions (42 total position components for the 2005 event), which effectively boosts the signal-to-noise ratio in the estimated slip.

6.1. Methods

[61] The Kalman filter method of *Cervelli et al.* [2002] directly estimates the time evolution of slip from raw double-differenced ionosphere-free carrier phase, Φ (t), and pseudorange $P(t)$ observations [e.g., *Hoffmann-Wellenhof et al.*, 1990]. Given the small station displacements due to the slow slip events, kinematic station positions are likely dominated by multipath, caused by the GPS signals reflecting off of the ground or nearby structures, and perhaps unmodeled atmospheric delays. These error sources obscure the tectonic signals. The GPS carrier phase and pseudorange observables, sampled every 30 s, are modeled as

$$\Phi(t) - r_o(t) = A\delta\mathbf{x}(t) + z(t)m_w + \lambda N \qquad (11)$$

$$P(t) - r_o(t) = A\delta\mathbf{x}(t) + z(t)m_w \qquad (12)$$

where r_o are the predicted double-differenced ranges from the stations to the satellites, the matrix, A, of partial derivatives relate the double-differenced ranges to corrections in the station coordinates, $\delta\mathbf{x}(t)$, which vary through time, z is the time-varying tropospheric zenith delay, m_w is a tropospheric mapping function and N are the sums of the integer phase ambiguities at the two GPS frequencies with wavelength λ. Cycle slips in the phase ambiguities are detected and flagged in advance so that N can be reset within the Kalman filter at the times they occur; pseudoranges are unambiguous. We solve directly for a scalar slip, $s(t)$, by substituting in the homogeneous elastic half space Green's functions, G, from the best fitting uniform slip fault:

$$\delta\mathbf{x}(t) = Gs(t). \qquad (13)$$

$s(t)$ is allowed to vary as a random walk in time, scaled by σ_s, which is chosen by trial and error such that the full amount of static slip, determined from the daily solutions in section 5, accumulates while still limiting scatter during the days preceding and following the transient deformation.

6.2. Subdaily Slip Model

[62] The time-dependent inversions show that for the 1998, 2000, and 2005 events, the slow slip events last from
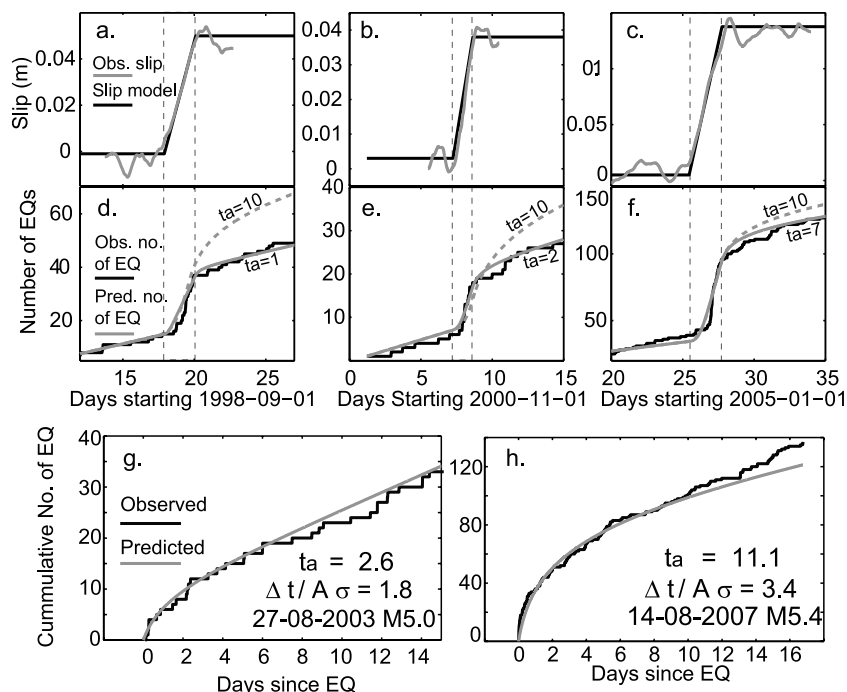
Figure 17. (a–c) Time-dependent slip models and simplified ramp functions for three of the largest slow slip events with significant seismicity increases (September 1998, November 2000, and January 2005). (d–f) Comparison of observed and theoretical aftershock behavior for these three slow slip events. (g and h) Observed and predicted seismicity rates and the estimates of characteristic aftershock decay time, t_a, for two regular M > 5 earthquakes.

1.5–2.2 days (Figures 17a–17c), summarized in Table 2. Each of the events also appears to follow a similar slip evolution that is well-approximated by a ramp function. To investigate whether slip migrated east-west or north-south during the largest 2005 event, we divided the south flank in two halves (E-W and N-S separately), and used the same inversion procedure to determine whether one patch slipped before the other. In both cases, the temporal pattern was the same as the single patch models (Figure 17a) for both patches, although the total magnitude of slip on the individual patches in each case was slightly different. Thus, at this point, we are unable to resolve any propagation of the slow slip.

7. Seismic Data

[63] Although slow slip events in Cascadia and Japan are associated with nonvolcanic tremor [e.g., *Rogers and Dragert*, 2003; *Hirose and Obara*, 2006], the most prominent seismic observation accompanying the Kilauea slow slip events is actually a sequence of small conventional (high-frequency) earthquakes [*Segall et al.*, 2006; *Brooks et al.*, 2006]. The arrival times and catalog locations of earthquakes are archived at the Hawaiian Volcano Observatory. We show here that the seismicity rates follow a temporal pattern

consistent with "coshock" and aftershock sequences resulting from the stress changes induced by the slow slip events.

7.1. Temporal Correlation With Slip

[64] Each of the larger slow slip events are accompanied by seismicity that occurs off the west and north edges of the imaged slow slip (Figure 16). The area around Poliokeawe Pali typically shows minor earthquake activity at a rate of 1–2 earthquakes per day. During the 1998, 2000, and 2003 silent slip events, seismic activity increased to 10–15 earthquakes per day (Figure 17a). The 2005 silent slip event, however, was accompanied by significantly higher seismicity rates of up to 58 earthquakes per day, again, in the same locations. All of these earthquakes are small; the largest being a M3.4 in 1998.

[65] In all cases, the cumulative moment of the microseismicity is far too small to account for the observed surface deformation. The cumulative moment of the 2005 swarm, which was the most energetic, is 1.8×10^{14} N-m, which is more than 3 orders of magnitude less than the moment of the slow slip, 6.8×10^{17} N-m, determined from the GPS data. A nearby swarm of microearthquakes occurred almost 2 weeks after the 1998 slow slip event, but produced no measurable surface displacement (Figure 17c, approximately day 27).

Table 2. Beginning, End, Duration, and Velocity of Each Slip Event

Start UTC (t_1, h)	End UTC (t_2, h)	Duration (days)	Slip (m)	Velocity (m a^{-1})
18 September 1998 ∼ 0000	20 September 1998 ∼ 0000	∼2	0.05	9.12
9 November 2000 ∼ 0000	10 November 2000 ∼ 1200	∼1.5	0.06	14.6
25 January 2005 ∼ 0000	28 January 2005 ∼ 0200	∼2.2	0.15	24.8

The cumulative moment of this swarm of 47 events was 2×10^{16} N-m, most of which was accounted for by a single $M_w 4.8$ (1.9×10^{16} N-m) event.

[66] Although the microearthquakes do not account for the surface deformation, the temporal association of the microearthquakes and the slow slip events suggests a causal relationship between them. This relationship can be explained by either (1) the earthquakes begin first and unpin the fault, allowing the slow slip to occur or (2) the slow slip begins first and stresses the adjacent fault, increasing the seismicity rate. With accurate determination of the slow slip timing, and quantitative modeling of the induced microseismicity, Segall et al. [2006] showed for the 2005 slow slip event that the second interpretation is supported by the slip model and seismicity rates. Therefore, the microearthquakes can be thought of as "coshocks" and aftershocks of the slow slip events.

[67] Using the slip evolution models obtained in section 6.2 and the accompanying microearthquake occurrences, we determine whether each swarm follows a similar temporal pattern that is consistent with the slip evolution. The slow slip and microearthquake swarms are quantitatively related using the seismicity rate theory of Dieterich [1994] as it was applied for the 2005 slow slip event in the work of Segall et al. [2006].

[68] Dieterich [1994] showed that the seismicity rate, R, is related to a background seismicity rate, r, the background stressing rate, $\dot{\tau}_r$, and a state variable, γ, as

$$R = \frac{dN}{dt} = \frac{r}{\gamma \dot{\tau}_r}, \tag{14}$$

where N is the number of earthquakes, and t is time. γ, a state variable, evolves with shear stress, τ and normal stress, σ, as

$$d\gamma = \frac{1}{a\sigma}[dt - \gamma d\tau + \gamma(\tau/\sigma - a)d\sigma]. \tag{15}$$

The cumulative number of expected microearthquakes, N, are computed for each event from a ramp function estimate of the slip model as given by Segall et al. [2006, equation 3]. The number of earthquakes depends on five parameters: (1) a characteristic aftershock decay time, t_a, which can be computed from prior regular earthquakes; (2) the background seismicity rate of 1.33 events d^{-1}; (3) the ratio of event stressing rate to background stressing rate; and (4) the onset and (5) the duration of the slow slip event. Only a change in the ratio of stressing rates, which determines the number of triggered events, requires estimation.

[69] Dieterich [1994] showed that characteristic aftershock decay times are given by the ratio of the fault constitutive parameter and the normal stress, to the background stressing rate, $t_a = A\sigma/\dot{\tau}_R$. We compute decay times on the basis of estimates from seven M > 5 earthquakes on Kilauea's southern flank, all of which occurred in the last 25 years at depths of 9 km between the East Rift Zone and the Hilina Pali. The earthquakes occur primarily in two clusters. One cluster is to the south of Pu'u 'O'o near the M5.1 used by Segall et al. [2006], and also includes the 1989 M6.2 South Flank earthquake (t_a = 19.3 days), and a 2007 M5.4 earthquake (t_a = 11.1 days). Each of the earthquakes in this cluster have upward of 40 aftershocks. In a second cluster to the

south of the bend in the ERZ, the character of the aftershocks changes significantly, with each event having fewer than 15 aftershocks. This cluster includes a 1989 M5.3 (t_a = 0.2 days), and two M5.0 earthquakes in 2000 and 2003 (t_a = 2.2 and 1.7 days, respectively). One M5.1 event in 1983 occurred south of Makaopuhi with an aftershock decay time of 7.1 days. We note that these aftershock decay times are shorter than those found by Dieterich [1994] and Dieterich et al. [2003]; however, we are more concerned with fitting the aftershock rates immediately during and following an event than the longer-term decay rates.

[70] Quantitatively relating the slow slip and seismicity, with parameter values shown in Figure 17, shows that the microearthquakes accompanying all of the modeled slow slip events follow a temporal pattern consistent with the seismicity being coshocks and aftershocks of their respective slow slip events. While Segall et al. [2006] used t_a = 10 days on the basis of one earthquake, improved fits are obtained using shorter characteristic aftershock decay times of 7 days for the 2005 event and still shorter times of 1–2 days for the 1999 and 2000 slow slip events. These shorter times are still within range of decay times observed above for M > 5 earthquakes on Kilauea. The 2005 event, which is the largest event and produced the most coshocks and aftershocks, a factor of 33 increase in stressing rate provides satisfactory agreement with the observed seismicity rates (Figure 17) [Segall et al., 2006]. An increase in stressing rate closer to a factor of 10 provides the best fit to the 1998 and 2000 slow slip events (Figure 17).

[71] The variation in aftershock decay times observed is consistent with Klein et al. [2006], who showed that short aftershock durations on Kilauea's south flank are typical of regular earthquakes and result from high background stress rates. The slip during the 1998 and 2000 slow slip events was concentrated to the west of the 2005 event, and closer to the cluster of earthquakes with the shorter characteristic aftershock decay times. The 2005 slow slip event had a broader slip distribution including the eastern part of the GPS network south of Pu'u 'O'o, which extended nearer to the regular earthquakes that produce more aftershocks and longer characteristic aftershock decay times. We believe that the shorter aftershock decay times required to better model the seismicity rates in 1998 and 2000 are consistent with previous regular earthquakes in their respective locations.

7.2. Relocation of Microearthquakes

[72] To use microearthquakes to help constrain the depth of the slow slip events, we need very precise locations. Catalog locations for most south flank earthquakes are distributed over a wide range of depths (5–12 km), but relocations show that they illuminate a subhorizontal plane [Got and Okubo, 2003; Hansen et al., 2004; Wolfe et al., 2007]. Wolfe et al. [2007] used full waveform cross correlations to relocate a set of earthquakes around three slow slip events (January 2005, September 1998, and November 2000). They found that the earthquakes collapsed onto horizontally aligned streaks from 4.5–6.5 km deep. Wolfe et al. [2007], who use only relative travel times, express concern over whether poor station geometry and velocity heterogeneity may bias their depth estimates. Here we relocate the coshocks and aftershocks of the largest slow slip events using both relative and absolute phase arrivals to constrain their depths.
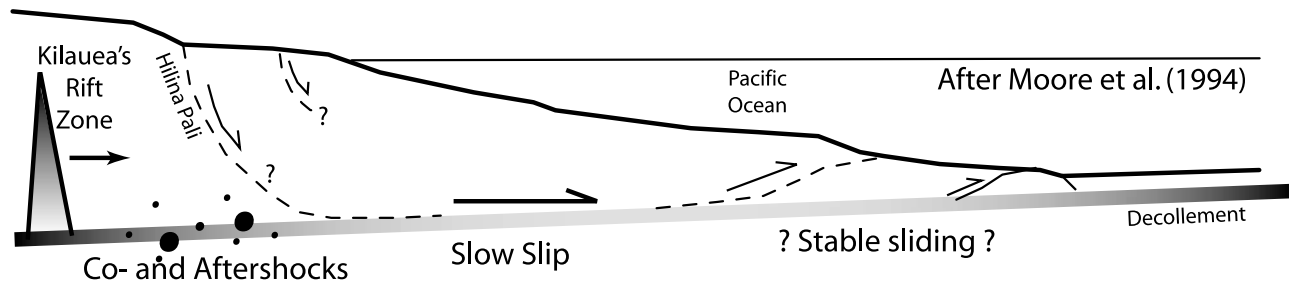
Figure 18. Schematic cross section of Kilauea Volcano showing the lateral relationship between the slow slip events and their aftershock locations. South flank tectonic structure adapted from *Moore et al.* [1994, Figure 6].

[73] Since the slow slip coshocks and aftershocks were only observed by the Hawaiian Volcano Observatory's backbone seismic network, we relocated them jointly with a subset of south flank microearthquakes very precisely located by *Hansen et al.* [2004]. *Hansen et al.* [2004] deployed a temporary network of 29 three-component seismometers from November 1999 to June 2000 aligned roughly perpendicular to the East Rift Zone. Using the temporary network, in addition to the Hawaiian Volcano Observatory permanent network, *Hansen et al.* [2004] jointly inverted for earthquake hypocenters and the three dimensional velocity structure. They found that the earthquakes between the East Rift Zone and the Palis lie on a nearly horizontal surface at a depth of 7–9 km. Although the temporary network was not deployed during any of the slow slip events, we can use the differential travel times between the *Hansen et al.* [2004] events and the slow slip swarm events to constrain the velocity structure and obtain absolute relocations for the swarm events accompanying the slow slip episodes.

[74] For this inversion, we do a full three-dimensional simultaneous double-difference relocation and tomography [*Zhang and Thurber*, 2003] including the coshocks and aftershocks of the largest slow slip events (September 1998, November 2000, July 2003, and January 2005), and the events detected during the *Hansen et al.* [2004] temporary deployment. With these five sets of phase arrivals, we have 1,384 earthquakes. The arrival times for the slow slip coshocks and aftershocks were automatically picked by the Hawaiian Volcano Observatory and arrival times for the 1999–2000 events were provided by the University of Wisconsin. Differential arrival times are obtained by differencing the arrival times at common stations for event pairs with catalog locations within 10 km, resulting in 13,210 pairs with 150,315 P and 44,156 S differential times.

[75] We start with an initial one-dimensional velocity model based on the results of *Hansen et al.* [2004]. Velocity nodes are spaced every 2 km in the horizontal and every 2 km in depth down to 10 km, plus nodes at 15 and 20 km. Far field grid nodes in the horizontal directions are at ±200 km and at a depth of 300 km. The 71 seismic stations are all on the Island of Hawaii within 40 km of Kilauea's caldera, which include the 29 temporary stations from the 1999–2000 [*Hansen et al.*, 2004] study. The deepest earthquake contributing to the velocity inversion is at 51 km, with 62 events deeper than 15 km.

[76] The aftershocks triggered by the slow slip events collapse onto a horizontal band between 6.5–8.5 km

(Figure 16). Most are clustered between the rift zone and the Palis, but there is a streak that extends south of the Palis and into the slow slip areas (Figure 16). The relative epicenters of these earthquakes are consistent with the results of *Wolfe et al.* [2007], but are deeper, possibly because of the differing velocity models, and the differences between relocations using only relative travel times, versus those including both relative and absolute arrivals. The weighted RMS errors for the catalog data improve from 606 to 58 ms following relocation. The overall structure and magnitude of the velocity model obtained (not shown) are very similar to the model of *Hansen et al.* [2004]. Location errors can be estimated using the jackknife method [e.g., *Waldhauser and Ellsworth*, 2000] in which several relocations are performed while eliminating a different seismic station from each inversion. Mean standard deviations of shifts from the estimated relocations including all seismic stations are 0.08 km in the East, 0.09 km in the North, and 0.11 km for the vertical, while maximum shifts are 1.31 km, 1.2 km, and 1.72 km respectively. The inclusion of the 1999–2000 data during the augmented deployment of *Hansen et al.* [2004] and the qualitative similarity to their velocity model provide additional confidence in the absolute depths of the events, to which we compare the optimal geodetically determined depths of slow slip events in Figure 14.

8. Discussion

[77] Displacements from the Kilauea slow slip events and large flank earthquakes (e.g., M7.2 1975 Kalapana earthquake) occur in the same horizontal direction as the steady-state velocities, not as a reversal of motion, as in subduction zone events. This is likely because of the difference in driving forces between subduction and volcanic spreading. In the simplest sense, subduction zone fault slip is driven by the colliding plates, where strain is accumulated on a locked part of the subduction fault and released during megathrust earthquakes. The slow slip events, however, complicate this view in that some of the compressional strain accumulates on a portion of the fault down-dip of the locked zone. This down-dip strain is periodically transferred to the locked zone during slow slip events. On Kilauea, the geometry is more landslide-like where gravity drives the seaward sliding of the south flank [*Moore et al.*, 1994]. The seismically active zone on Kilauea between the rift and the Palis may slip in large flank earthquakes, like the 1975 M7.2 Kalapana earthquake, but perhaps structural features on Kilauea, like the Hilina Pali faults, influence the locations of the slow slip events

(Figure 18). However, there have been no reports of surface offsets on the Palis due to the slow slip events.

[78] The November 2000 slow slip event on Kilauea was associated with an unusually large rainfall event possibly influencing the slip with an increased surface load and reduction of the effective normal stress due to pore pressure from infiltrated water [*Cervelli et al.*, 2002]. However, other slow slip events have not been associated with elevated rainfall [*Brooks et al.*, 2006] requiring another mechanism for generating slip. Many proposed mechanisms for generating slow slip require reduced effective normal stresses, most likely because of high fluid pressures [*Liu and Rice*, 2007]. Ignoring pore fluid, which may be important beneath Kilauea's south flank, the 300 m elevation difference across the Palis translates to a 10 MPa normal stress difference between the slow slip regions and the seismic regions just to the north. However, a deep water table may exist, while overpressured pore fluids may also be present within the sediment layer at the base of the volcano.

[79] Locations of slow slip events in subduction zones are often explained by the presumed presence of metamorphic fluids lowering the effective normal stress. The source of the fluids in subduction zones is suggested to be metamorphic mineral phase transition to eclogite [*Obara et al.*, 2004] at subduction zone temperatures and pressures. However, phase diagrams [*Peacock and Wang*, 1999] show that most of these reactions occur at high pressures and therefore greater depths that are not reached on Kilauea's decollement. One possibility for providing fluid to lower the effective normal stress at Kilauea is simply the collapse of pelagic sediment porosity. Expelling pore fluid can occur at much lower P-T conditions than mineral phase transitions (0–20 km, <200°C for models in Cascadia) and produces 5–10 times the fluid flux of the mineral phase transitions [*Hyndman and Peacock*, 2003]. *Hyndman and Peacock* [2003] assumed sediment thickness of 1000 m and porosity of 7% for the oceanic slab in Cascadia on the basis of Ocean Drilling Program measurements. Pelagic sediment thicknesses offshore of Kilauea are closer to 80–100 m [*Leslie et al.*, 2002].

[80] Unlike slow slip events in Japan and Cascadia [*Obara et al.*, 2004; *Rogers and Dragert*, 2003], the Hawaiian events have not yet been correlated with nonvolcanic tremor. However, very few continuous seismic waveforms are available for the larger Kilauea slow slip events, and many stations are "contaminated" by volcanic tremor from the active eruption. Tremor also has not been detected during slow slip events in the Hikurangi subduction zone of New Zealand after an extensive search of waveforms from their dense seismic array; however, the slow slip events have been shown to correlate with seismic swarms [*Delahaye et al.*, 2008], similar to what is observed on Kilauea. The shallow locking depth (<20 km) and very cool temperatures (100–150°C) of the Hikurangi subduction zone may be the most similar subduction zone analog to P-T conditions on Kilauea's decollement at their respective transition zones. While some phase transitions may be occurring, neither Kilauea nor New Zealand reaches the high pressures required for transition to initiate dehydration reactions that release significant water at the high lithostatic pressures at 350–450 km depths of the Japan and Cascadia subduction zone slow slip and nonvolcanic tremor events [*Hyndman and Peacock*, 2003].

The phase transitions are thus not likely primary fluid sources on Kilauea.

[81] The apparent periodicity of the four large events prompted a collaborative effort to instrument the south flank of Kilauea Volcano in anticipation of an event in mid-March of 2007. The new deployment included two permanent tiltmeters, nine short-period seismometers, three broadband seismometers, and several high-rate GPS stations. As of this writing, there was a dike intrusion in June 2007 with some indication that the anticipated slow slip event occurred during the intrusion [*Brooks et al.*, 2008], but additional work is still in progress [*Montgomery-Brown et al.*, 2007]. If the intrusion did not alter the overall system, and the apparent 2-year periodicity of the larger events continues, it is possible that another event may occur in 2009.

9. Conclusions

[82] The major conclusions about the Kilauea slow slip events can be summarized as follows:

[83] 1. One new slow slip event (29 May 2000) was detected by searching for displacement patterns similar to previously identified events, with supporting evidence from increased seismicity during the event. Four other events had similar displacement fields to the references, but were very small and did not correlate with increased seismicity, and thus remain ambiguous. The eight confirmed slow slip events (plus the June 2007 combination intrusion/slow slip event not studied here) do not appear to follow either a periodic, slip-predictable, nor time-predictable model.

[84] 2. Microearthquakes during and following all of the large slow slip events have been relocated; the events collapse to a band 6.5–8.5 km deep.

[85] 3. Including the effects of topography and layered elastic structure reconciles the range of acceptable depths for the Kilauea slow slip events with the depths of the inferred aftershocks to a depth range between 6.5–8.5 km, further supporting the suggestion that the slow slip events and their aftershocks are occurring on the decollement beneath Kilauea.

[86] 4. Subdaily slip models for the 1998, 2000, and 2005 slow slip events show similar temporal evolutions, with each event lasting 1.5–2 days. There is no indication of slip migration, but migration may not be resolvable with the current GPS network.

[87] 5. Relating the slip histories of the 1998, 2000, and 2005 slow slip events to their accompanying microearthquake swarms shows that the microearthquakes are consistent with the predicted temporal evolution of coshock and aftershock sequences, assuming a rate- and state-dependent friction model.

References

Altamimi, Z., X. Collilieux, J. Legrand, B. Garayt, and C. Boucher (2007), ITRF2005: A new release of the international terrestrial reference frame

based on time series of station positions and Earth orientation parameters, *J. Geophys. Res.*, *112*, B09401, doi:10.1029/2007JB004949.

Anderson, T. (2003), *An Introduction to Multivariate Statistical Analysis*, chap. 2.3, John Wiley, Hoboken, N. J.

Ando, M. (1979), The Hawaii earthquake of November 1975: Low dip angle faulting due to forceful injection of magma, *J. Geophys. Res.*, *84*, 7616–7626.

Borgia, A. (1994), Dynamic basis of volcanic spreading, *J. Geophys. Res.*, *99*, 17,791–17,804.

Brooks, B., J. Foster, D. Sandwell, M. Poland, D. Myer, C. Wolfe, and M. Patrick (2007), Quasi-periodic slow earthquakes and their association with magmatic activity at Kilauea Volcano, Hawai'i, *Eos Trans. AGU*, *88*(52), Fall Meet. Suppl., Abstract T12C-07.

Brooks, B., J. Foster, D. Sandwell, C. Wolfe, P. Okubo, M. Poland, and D. Myer (2008), Magmatically triggered slow slip at Kilauea Volcano, Hawaii, *Science*, *321*(5893), 1177, doi:10.1126/science.1159,007.

Brooks, B. A., J. H. Foster, M. Bevis, L. N. Frazer, C. J. Wolfe, and M. Behn (2006), Periodic slow earthquakes on the flank of Kilauea Volcano, Hawai'i, *Earth Planet. Sci. Lett.*, *246*(3/4), 207–216, doi:10.1016/j.epsl.2006.03.035.

Brudzinski, M., and R. Allen (2007), Segmentation in episodic tremor and slip all along Cascadia, *Geology*, *35*(10), 907–910, doi:10.1130/G23740A.1.

Bufe, C., P. Harsh, and R. Burford (1977), Steady-state seismic slip: A precise recurrence model, *Geophys. Res. Lett.*, *4*(2), 91–94.

Cannon, E. C., R. Burgmann, and S. E. Owen (2001), Shallow normal faulting and block rotation associated with the 1975 Kalapana earthquake, Kilauea Volcano, Hawaii, *Bull. Seismol. Soc. Am.*, *91*(6), 1553–1562.

Cayol, V., and F. H. Cornet (1998), Effects of topography on the interpretation of the deformation field of prominent volcanoes: Application to Etna, *Geophys. Res. Lett.*, *25*(11), 1979–1982.

Cervelli, P., P. Segall, K. Johnson, M. Lisowski, and A. Miklius (2002), Sudden aseismic fault slip on the south flank of Kilauea Volcano, *Nature*, *415*(6875), 1014–1018.

Delahaye, E. J., J. Townend, M. E. Reyners, and G. Rogers (2008), Microseismicity but no tremor accompanying slow slip in the Hikurangi subduction zone, New Zealand, *Earth Planet. Sci. Lett.*, *277*(1–2), 21–28.

Delaney, P., R. Denlinger, M. Lisowski, A. Miklius, P. Okubo, A. Okamura, and M. Sako (1998), Volcanic spreading at Kilauea, 1976–1996, *J. Geophys. Res.*, *103*, 18,003–18,023.

Dieterich, J. (1994), A constitutive law for rate of earthquake production and its application to earthquake clustering, *J. Geophys. Res.*, *99*, 2601–2618.

Dieterich, J., V. Cayol, and P. Okubo (2003), Stress changes before and during the Pu'u 'Ō'ō-Kūpianaha eruption, *U.S. Geol. Surv. Prof. Pap.*, *1676*, 187–202.

Dragert, H., K. Wang, and G. Rogers (2004), Geodetic and seismic signatures of episodic tremor and slip in the northern Cascadia subduction zone, *Earth Planets Space*, *56*(12), 1143–1150.

Furumoto, A. S., and R. L. Kovach (1979), The Kalapana earthquake of November 29, 1975: An intra-plate earthquake and its relation to geothermal processes, *Phys. Earth Planet. Interiors*, *18*(3), 197–208.

Got, J.-L., and P. Okubo (2003), New insights into Kilauea's Volcano dynamics brought by large scale relative relocation of microearthquakes, *J. Geophys. Res.*, *108*(B7), 2337, doi:10.1029/2002JB002060.

Hansen, P. (1992), Analysis of discrete ill-posed problems by means of the L-curve, *SIAM Rev.*, *34*(4), 561–580.

Hansen, S., C. Thurber, M. Mandernach, F. Haslinger, and C. Doran (2004), Seismic velocity and attenuation structure of the east rift zone and south flank of Kilauea Volcano, Hawaii, *Bull. Seismol. Soc. Am.*, *94*(4), 1430–1440.

Heki, K., and S. Miyazaki (2001), Plate convergence and long-term crustal deformation in central Japan, *Geophys. Res. Lett.*, *28*(12), 2313–2316.

Hill, D., and J. Zucca (1987), Geophysical constraints on the structure of Kilauea and Mauna Loa volcanoes and some implications for seismo-magmatic processes, in *Volcanism in Hawaii*, *U.S. Geol. Surv. Prof. Pap.*, *1350*, vol. 2, edited by R. Decker, T. Wright, and P. Stauffer, pp. 903–917.

Hill, D. P. (1969), Crustal structure of the island of Hawaii from seismic-refraction measurements, *Bull. Seismol. Soc. Am.*, *59*(1), 101–130.

Hirose, H., and K. Obara (2006), Short-term slow slip and correlated tremor episodes in the Tokai region, central Japan, *Geophys. Res. Lett.*, *33*, L17311, doi:10.1029/2006GL026579.

Hirose, H., K. Hirahara, F. Kimata, N. Fujii, and S. Miyazaki (1999), A slow thrust slip event following the two 1996 Hyuganada earthquakes beneath the Bungo Channel, southwest Japan, *Geophys. Res. Lett.*, *26*(21), 3237–3240.

Hoffmann-Wellenhof, B., H. Lichtenegger, and J. Collins (1990), *GPS: Theory and Practice*, Cambridge Univ. Press, Cambridge, U. K.

Hooper, A., P. Segall, and H. Zebker (2007), Persistent scatterer interferometric synthetic aperture radar for crustal deformation analysis, with application to Volcan Alcedo, Galapagos, *J. Geophys. Res.*, *112*, B07407, doi:10.1029/2006JB004763.

Hyndman, R., and S. Peacock (2003), Serpentinization of the forearc mantle, *Earth Planet. Sci. Lett.*, *212*, 417–432.

Ide, S., D. R. Shelly, and G. C. Beroza (2007), Mechanism of deep low frequency earthquakes: Further evidence that deep non-volcanic tremor is generated by shear slip on the plate interface, *Geophys. Res. Lett.*, *34*, L03308, doi:10.1029/2006GL028890.

Kao, H., S. J. Shan, H. Dragert, G. Rogers, J. F. Cassidy, and K. Ramachandran (2005), A wide depth distribution of seismic tremors along the northern Cascadia margin, *Nature*, *436*(7052), 841–844.

Klein, F., Y. Koyanagi, J. Nakata, and W. Tanigawa (1987), The seismicity of Kilauea's magma system., in *Volcanism in Hawaii*, *U.S. Geol. Surv. Prof. Pap.*, vol. 1350, edited by R. Decker, T. Wright, and P. Stauffer, pp. 1019–1185.

Klein, F., T. Wright, and J. Nakata (2006), Aftershock decay, productivity, and stress rates in Hawaii: Indicators of temperature and stress from magma sources, *J. Geophys. Res.*, *111*, B07307, doi:10.1029/2005JB003949.

Kostoglodov, V., S. K. Singh, J. A. Santiago, S. I. Franco, K. M. Larson, A. R. Lowry, and R. Bilham (2003), A large silent earthquake in the Guerrero seismic gap, Mexico, *Geophys. Res. Lett.*, *30*(15), 1807, doi:10.1029/2003GL017219.

Larson, K., A. R. Lowry, V. Kostoglodov, W. Hutton, O. Sanchez, K. Hudnut, and G. Suarez (2004), Crustal deformation measurements in Guerrero, Mexico, *J. Geophys. Res.*, *109*, B04409, doi:10.1029/2003JB002843.

Leslie, S., G. M. J. Morgan, and D. Hills (2002), Seismic stratigraphy of the frontal Hawaiian moat: Implications for sedimentary processes at the leading edge of an oceanic hotspot trace, *Mar. Geol.*, *184*, 143–162.

Lipman, P., J. Lockwood, R. Okamura, D. Swanson, and K. Yamashita (1985), Ground deformation associated with the 1975 magnitude-7.2 earthquake and resulting changes in activity of Kilauea Volcano, Hawaii, *U. S. Geol. Surv. Prof. Pap.*, *1276*, 1–45.

Lipman, P., T. Sisson, M. Coombs, A. Calvert, and J. Kimura (2006), Piggyback tectonics: Long-term growth of Kilauea on the south flank of Mauna Loa, *J. Volcanol. Geotherm. Res.*, *51*, 73–108, doi:10.1016/j.jvolgeores.2005.07.032.

Liu, Y. J., and J. R. Rice (2007), Spontaneous and triggered aseismic deformation transients in a subduction fault model, *J. Geophys. Res.*, *112*, B09404, doi:10.1029/2007JB004930.

Lowry, A. R., K. M. Larson, V. Kostoglodov, and R. Bilham (2001), Transient fault slip in Guerrero, southern Mexico, *Geophys. Res. Lett.*, *28*(19), 3753–3756.

McTigue, D. F., and P. Segall (1988), Displacements and tilts from dip-slip faults and magma chambers beneath irregular surface topography, *Geophys. Res. Lett.*, *15*(6), 601–604.

Metropolis, N., A. Rosenbluth, M. Rosenbluth, A. Teller, and E. Teller (1953), Equation of state calculations by fast computing machines, *J. Chem. Phys.*, *21*, 1087–1092.

Miklius, A., P. Cervelli, M. Sako, M. Lisowski, S. Owen, P. Segal, J. Foster, K. Kamibayashi, and B. Brooks (2005), Global positioning system measurements on the Island of Hawai'i: 1997 through 2004, *U.S. Geol. Surv. Open File Rep.*, *2005-1425*, 48 pp.

Miller, M. M., T. Melbourne, D. J. Johnson, and W. Q. Sumner (2002), Periodic slow earthquakes from the Cascadia subduction zone, *Science*, *295*(5564), 2423–2423.

Miyazaki, S., J. McGuire, and P. Segall (2003), A transient subduction zone slip episode in southwest Japan observed by the nationwide GPS array, *J. Geophys. Res.*, *108*(B2), 2087, doi:10.1029/2001JB000456.

Miyazaki, S., P. Segall, J. J. McGuire, and T. Kato (2006), Spatial and temporal evolution of stress and slip rate during the 2000 Tokai slow earthquake, *J. Geophys. Res.*, *111*, B03409, doi:10.1029/2004JB003426.

Mogi, K. (1958), Relations between the eruptions of various volcanoes and the deformations of the ground surfaces around them, *Bull. Earthquake Res. Inst. Univ. Tokyo*, *36*, 111–123.

Montgomery-Brown, E., D. Sinnett, P. Segall, A. Miklius, M. Poland, and K. Larson (2007), Source models of the June 17, 2007 intrusion at Kilauea Volcano, Hawaii: Spatio-temporal evolution, *EOS, Trans. AGU*, *88*(52), Fall Meet. Suppl., Abstract V52A-1138.

Moore, J. (2001), Density of basalt core from Hilo drill hole, Hawaii, *J. Volcanol. Geotherm. Res.*, *112*, 221–230.

Moore, J. G., W. R. Normark, and R. T. Holcomb (1994), Giant Hawaiian landslides, *Annu. Rev. Earth Planet. Sci.*, *22*, 119–144.

Morgan, J., and P. McGovern (2003), Discrete element simulations of volcanic spreading: Implications for the structure of Olympus Mons, *Lunar Planet. Sci.*, *XXXIV*, Abstract 2088.

Morgan, J. K., G. F. Moore, D. J. Hills, and S. Leslie (2000), Overthrusting and sediment accretion along Kilauea's mobile south flank, Hawaii: Evidence for volcanic spreading from marine seismic reflection, *Geology*, *28*(7), 667–670, doi:10.1130/0091-7613(2000)28<667:OASAAK>2.0.CO;2.

Obara, K., H. Hirose, F. Yamamizu, and K. Kasahara (2004), Episodic slow slip events accompanied by non-volcanic tremors in southwest Japan subduction zone, *Geophys. Res. Lett.*, *31*, L23602, doi:10.1029/2004GL020848.

Okada, Y. (1985), Surface deformation due to shear and tensile faults in a half-space, *Bull. Seismol. Soc. Am.*, *75*, 1135–1154.

Okubo, P. G., H. M. Benz, and B. A. Chouet (1997), Imaging the crustal magma sources beneath Mauna Loa and Kilauea volcanoes, Hawaii, *Geology*, *25*(10), 867–870.

Owen, S., and R. Burgmann (2006), An increment of volcano collapse: Kinematics of the 1975 Kalapana, Hawaii, earthquake, *J. Volcanol. Geothermal Res.*, *150*, 163–185, doi:10.1016/j.jvolgeores.2005.07.012.

Owen, S., P. Segall, M. Lisowski, A. Miklius, R. Denlinger, and M. Sako (2000a), Rapid deformation of Kilauea Volcano: Global positioning system measurements between 1990 and 1996, *J. Geophys. Res.*, *105*, 18,983–18,998.

Owen, S., P. Segall, M. Lisowski, A. Miklius, M. Murray, M. Bevis, and J. Foster (2000b), January 30, 1997 eruptive event on Kilauea Volcano, Hawaii, as monitored by continuous GPS, *Geophys. Res. Lett.*, *27*(17), 2757–2760.

Ozawa, S., M. Murakami, and T. Tada (2001), Time-dependent inversion study of the slow thrust event in the Nankai trough subduction zone, southwestern Japan., *J. Geophys. Res.*, *106*, 787–802.

Ozawa, S., Y. Hatanaka, M. Kaidzu, M. Murakami, T. Imakiire, and Y. Ishigaki (2004), Aseismic slip and low-frequency earthquakes in the Bungo channel, southwestern Japan, *Geophys. Res. Lett.*, *31*, L07609, doi:10.1029/2003GL019381.

Payero, J., V. Kostoglodov, T. Mikumo, X. Perez-Campos, A. Iglesias, and R. Clayton (2008), Nonvolcanic tremors in the Mexican subduction zone, *Geophys. Res. Lett.*, *35*, L07305, doi:10.1029/2007GL032877.

Peacock, S., and K. Wang (1999), Seismic consequences of warm versus cool subduction metamorphism: Examples from southwest and northeast Japan, *Science*, *286*(5441), 937–939.

Phillips, K. A., and C. D. Chadwell (2004), Results of seafloor vertical deformation montoring on the submerged south flank of Kilauea Volcano, Hawaii from 2000 to 2004, *EOS, Trans. AGU*, *85*(47), Fall Meet. Suppl., Abstract G51A-0053.

Rogers, G., and H. Dragert (2003), Episodic tremor and slip on the Cascadia subduction zone: The chatter of silent slip, *Science*, *300*(5627), 1942–1943.

Schwartz, S., and J. Rokosky (2007), Slow slip events and seismic tremor at circum-Pacific subduction zones, *Rev. Geophys.*, *45*, RG3004, doi:10.1029/2006RG000208.

Segall, P. (2009), *Earthquake and Volcano Deformation*, Princeton Univ. Press, Princeton, N. J., in press.

Segall, P., E. Desmarais, D. Shelly, A. Miklius, and P. Cervelli (2006), Earthquakes triggered by silent slip events on Kilauea Volcano, Hawaii, *Nature*, *442*, doi:10.1038/nature04938.

Shelly, D. R., G. C. Beroza, S. Ide, and S. Nakamula (2006), Low-frequency earthquakes in Shikoku, Japan, and their relationship to episodic tremor and slip, *Nature*, *442*(7099), 188–191, doi:10.1038/nature04931.

Shimazaki, K., and T. Nakata (1980), Time-predictable recurrence model for large earthquakes, *Geophys. Res. Lett.*, *7*(4), 279–282.

Swanson, D. A., W. A. Duffield, and R. S. Fiske (1976), Displacement of the south flank of Kilauea Volcano, Hawaii: The result of forceful intrusion of magma into the rift zones, *U.S. Geol. Surv. Prof. Pap.*, *963*, 39 pp.

Szeliga, W., T. Melbourne, M. Miller, and V. Santillan (2004), Southern Cascadia episodic slow earthquakes, *Geophys. Res. Lett.*, *31*, L16602, doi:10.1029/2004GL020824.

Thatcher, W. (2001), Silent slip on the Cascadia subduction interface, *Science*, *292*(5521), 1495–1496, doi:10.1126/science.1061770.

Waldhauser, F., and W. L. Ellsworth (2000), A double-difference earthquake location algorithm: Method and application to the northern Hayward fault, California, *Bull. Seismol. Soc. Am.*, *90*(6), 1353–1368, doi:10.1785/0120000006.

Williams, C. A., and G. Wadge (1998), The effects of topography on magma chamber deformation models: Application to Mt. Etna and radar interferometry, *Geophys. Res. Lett.*, *25*(10), 1549–1552, doi:10.1029/98GL01136.

Williams, C. A., and G. Wadge (2000), An accurate and efficient method for including the effects of topography in three-dimensional elastic models of ground deformation with applications to radar interferometry, *J. Geophys. Res.*, *105*, 8103–8120, doi:10.1029/1999JB900307.

Wolfe, C., B. Brooks, J. Foster, and P. Okubo (2007), Microearthquake streaks and seismicity triggered by slow earthquakes on the mobile south flank of Kilauea Volcano, Hawai'i, *Geophys. Res. Lett.*, *34*, L23306, doi:10.1029/2007GL031625.

Wyss, M. (1988), A proposed source model for the great Kau, Hawaii, earthquake of 1868, *Bull. Seismol. Soc. Am.*, *78*, 1450–1462.

Yoshioka, S., T. Mikumo, V. Kostoglodov, K. M. Larson, A. R. Lowry, and S. K. Singh (2004), Interplate coupling and a recent aseismic slow slip event in the Guerrero seismic gap of the Mexican subduction zone, as deduced from GPS data inversion using a Bayesian information criterion, *Phys. Earth Planet. Interiors*, *146*(3–4), 513–530.

Yun, S.-H., J. Ji, H. Zebker, and P. Segall (2005), On merging high- and low-resolution DEMs from TOPSAR and SRTM using a prediction-error filter, *IEEE Trans. Geosci. Remote Sens.*, *43*(7), 1682–1690.

Zhang, H., and C. Thurber (2003), Double-difference tomography: The method and its application to the Hayward Fault, California, *Bull. Seismol. Soc. Am.*, *93*(5), 1875–1889, doi:10.1785/0120020190.

Zumberge, J. F., M. B. Heflin, D. C. Jefferson, M. M. Watkins, and F. H. Webb (1997), Precise point positioning for the efficient and robust analysis of GPS data from large networks, *J. Geophys. Res.*, *102*, 5005–5017.

————————————

A. Miklius, Hawaiian Volcano Observatory, U.S. Geological Survey, Hawaii National Park, HI 96718, USA.

E. K. Montgomery-Brown and P. Segall, Department of Geophysics, Stanford University, Stanford, CA 94305, USA. (emilyd@stanford.edu)